Observations of Freezing Drizzle in Extratropical Cyclonic Storms during IMPROVE-2

KYOKO IKEDA, ROY M. RASMUSSEN, WILLIAM D. HALL, AND GREGORY THOMPSON

National Center for Atmospheric Research, Boulder, Colorado

(Manuscript received 9 June 2006, in final form 7 December 2006)

ABSTRACT

Observations of supercooled drizzle aloft within two storms impacting the Oregon Cascades during the second Improvement of Microphysical Parameterization through Observational Verification Experiment (IMPROVE-2) field project are presented. The storms were characterized by a structure and evolution similar to the split-front model of synoptic storms. Both storms were also characterized by strong cross-barrier flow. An analysis of aircraft and radar data indicated the presence of supercooled drizzle during two distinct storm periods: 1) the intrafrontal period immediately following the passage of an upper cold front and 2) the postfrontal period. The conditions associated with these regions of supercooled drizzle included 1) temperatures between $-3°$ and $-19°C$, 2) ice crystal concentrations between 1 and 2 L^{-1}, and 3) bimodal cloud droplet distributions of low concentration [cloud condensation nuclei (CCN) concentration between 20 and 30 cm^{-3} and cloud drop concentration <35 cm^{-3}].

Unique to this study was the relatively cold cloud top ($<-15°C$) and relatively high ice crystal concentrations in the drizzle region. These conditions typically hinder drizzle formation and survival; however, the strong flow over the mountain barrier amplified vertical motions (up to 2 m s^{-1}) above local ridges, the mountain crest, and updrafts in embedded convection. These vertical motions produced high condensate supply rates that were able to overcome the depletion by the higher ice crystal concentrations. Additionally, the relatively high vertical motions resulted in a near balance of ice crystal fall speed (0.5–1.0 m s^{-1}), leading to nearly terrain-parallel trajectories of the ice particles and a reduction of the flux of ice crystals from the higher levels into the low-level moisture-rich cloud, allowing the low-level cloud water and drizzle to be relatively undepleted.

One of the key observations in the current storms was the persistence of drizzle drops in the presence of significant amounts of ice crystals over the steepest portion of the mountain crest. Despite the high radar reflectivity produced by the ice crystals (>15 dBZ) in this region, the relatively high condensate supply rate led to hazardous icing conditions. The current study reveals that vertical motions generated by local topographic features are critical in precipitation processes such as drizzle formation and thus it is essential that microphysical models predict these motions.

1. Introduction

A number of recent field programs have focused on the meteorological conditions leading to in-flight aircraft icing: the Winter Icing and Storms Project (WISP; Rasmussen et al. 1992), the Canadian Freezing Drizzle Experiment (CFDE; Isaac et al. 1999), the National Aeronautics and Space Administration/Federal Aviation Administration/National Center for Atmospheric Research (NASA/FAA/NCAR) supercooled large droplet icing flight research (Miller et al. 1998), and the first and second Alliance Icing Research Study (AIRS; Isaac et al. 2001). These programs have primarily focused on aircraft icing conditions over relatively gentle terrain (e.g., eastern plains of Colorado, Newfoundland, and Cleveland) in association with cold fronts, warm fronts, and other features of midlatitude cyclones (Bernstein et al. 1997). One of the key results from these and other studies is the significantly higher frequency of supercooled or freezing drizzle[1] than previously thought (Cober et al. 2001). Supercooled drizzle aloft can be particularly hazardous to aircraft due to the impaction of these droplets beyond current deicing

Corresponding author address: Ms. Kyoko Ikeda, National Center for Atmospheric Research, P.O. Box 3000, Boulder, CO 80307.
E-mail: kyoko@ucar.edu

DOI: 10.1175/JAS3999.1

[1] Strictly speaking, drizzle drops are between 200 and 500 μm in diameter. However, in this paper we extend the size range down to 50 μm to include "embryo" drizzle drops.

boots, leading to a significant reduction in aircraft performance that cannot be alleviated by the activation of ice protection devices such as pneumatic boots (Sand et al. 1984; Telford 1988; Politovich 1989; Ashenden et al. 1996). Thus, understanding the environment in which supercooled drizzle forms is essential for forecasting and detecting this hazardous condition.

Previous field programs have shown that freezing drizzle is most commonly formed via a collision–coalescence process rather then the melting of ice crystals that subsequently fall into below-freezing air and form freezing rain (Rasmussen et al. 1995; Cober et al. 1996; Rauber et al. 2000). Recent surface climatologies of freezing drizzle found that freezing drizzle tends to maximize over the central Great Plains, Midwest, and near the Great Lakes in the United States—in association with gradual lifting of air masses mainly on the cool side of warm fronts associated with midlatitude cyclones (Bernstein et al. 1998; Bernstein 2000; Cortinas et al. 2004). Additionally, the above-surface climatologies have found freezing drizzle maxima over the Canadian Maritime Provinces, Newfoundland, and southeast Alaska in relation to maritime air masses. Furthermore, supercooled liquid drops aloft have been inferred from satellite observations and pilot reports (PIREPs) in these same regions, as well as the Pacific Northwest, Norway, the United Kingdom, Ireland, and some parts of Asia (B. C. Bernstein 2006, personal communication). These observations are consistent with conventional thinking in cloud physics that the production of precipitation-sized water drops through the collision–coalescence process is relatively rapid in maritime environments in which cloud condensation nuclei (CCN) concentrations are low, leading to rapid broadening of the cloud droplet spectra to sizes large enough for the collision–coalescence process to initiate.

The likelihood of freezing drizzle formation also increases when the cloud top is warmer than $-15°C$. For instance, Geresdi et al. (2005) found that 90% of freezing drizzle events at the ground level come from clouds with warm tops, greater than $-12°C$, based on the analysis of five years of upper-air sounding data over North America and surface precipitation reports (cf. their Figs. 3 and 4). This finding is consistent with in-cloud observations of supercooled drizzle by Politovich (1989), Murakami et al. (1992), and Cober et al. (1996), and surface-freezing drizzle observations by Rasmussen et al. (1995).

The above studies also suggested that icing conditions (the presence of freezing precipitation including supercooled liquid water) tends to be minimized when the equivalent radar reflectivity factor (hereafter reflectivity) is greater than 5 dBZ. Since drizzle drops typically produce reflectivities less than 5 dBZ with 10-cm wavelength radars (e.g., Ikeda et al. 2005b), a greater reflectivity typically indicates the presence of ice. Ice reduces supercooled liquid water and drizzle water content through depositional and accretional growth, thus limiting its buildup (Geresdi et al. 2005). Since vertical motions in many of the icing clouds observed in previous programs are <10 cm s^{-1} (Murakami et al. 1992; Cober et al. 1996; Rasmussen et al. 1995), it does not take much ice to significantly deplete the water as ice/snow particles descend through clouds. Consequently, freezing drizzle is generally not observed in regions in which ice crystal concentrations are greater than 0.1 L^{-1} (Rasmussen et al. 1995; Cober et al. 1996; Geresdi et al. 2005).

Icing diagnosis algorithms, such as the Current Icing Product (CIP; Bernstein et al. 2005) are based on much of the understanding discussed in the previous paragraphs. However, relatively few aircraft icing field programs have been conducted in regions of complex terrain, such as the Pacific Northwest, even though some weather modification studies have indicated the presence of freezing drizzle over the Sierra Nevada in California (e.g., Reynolds and Kuciauskas 1988; Rauber 1992). In this paper we describe observations of supercooled drizzle that produced in-flight icing during two extratropical cyclonic storms impacting the complex Oregon Cascades during the second Improvement of Microphysical Parameterization through Observational Verification Experiment (IMPROVE-2; Stoelinga et al. 2003). The goal of the IMPROVE-2 program, which took place in the west-central Oregon Cascades in November–December 2001, was to improve bulk microphysical parameterizations over regions of mountainous terrain in order to better predict precipitation in these critical regions. The observations of supercooled drizzle examined here will also be used as verification data for future numerical simulations of freezing drizzle and mixed-phase precipitation in these regions.

The two frontal systems examined in this study resembled the split-front conceptual model described by Browning and Monk (1982) (Fig. 1). Woods et al. (2005) defined five stages in precipitation associated with the 14 December 2001 storm—one of the storms examined in this study. They are 1) prefrontal showers, 2) an upper cold-frontal rainband, 3) intrafrontal convection, 4) surface-frontal precipitation, and 5) postfrontal convection. The split front is a katafront in which the upper dry cold front overruns the surface cold front leaving a moist shallow layer near the surface. Winter storms moving over the Sierra Nevada have been observed to follow the split-front conceptual model in many cases (e.g., Heggli and Reynolds 1985;

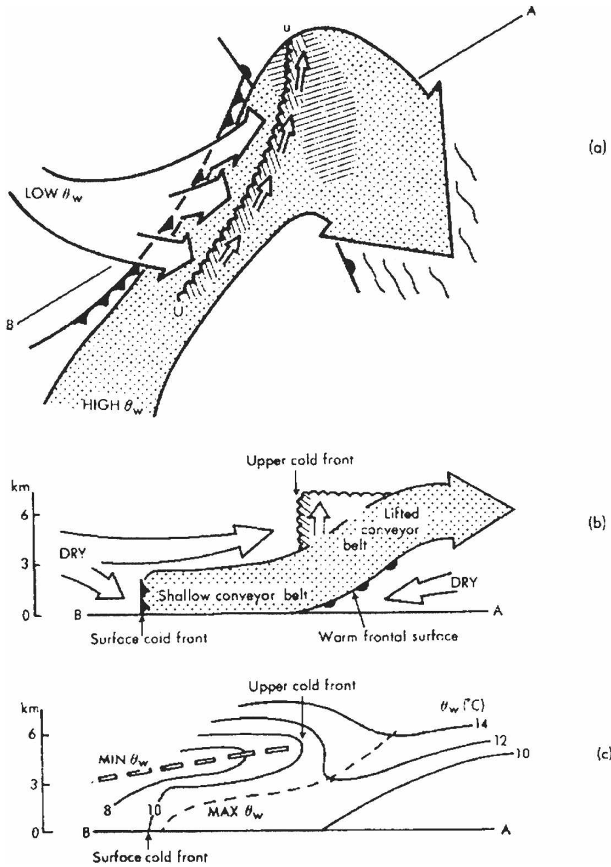

FIG. 1. Schematic of a katafront in (a) plan view and (b), (c) vertical section. The broad stippled arrow in (a) and (b) represents the high θ_w flow that, relative to the moving system, travels ahead of the surface cold front before rising and turning to the right above a warm-frontal zone. The arrows entering from the left of the diagrams represent dry air (low θ_w) that overruns the high-θ_w flow after having descended from the cold side of the upper-tropospheric jet stream. At the leading edge of the overrunning dry airflow, air ascends convectively from the top of the conveyor belt to generate a major rainband along the upper cold front (cusped line UU) that may extend from within the conventional warm sector to a position ahead of the surface warm front. (Courtesy of Browning and Monk 1982).

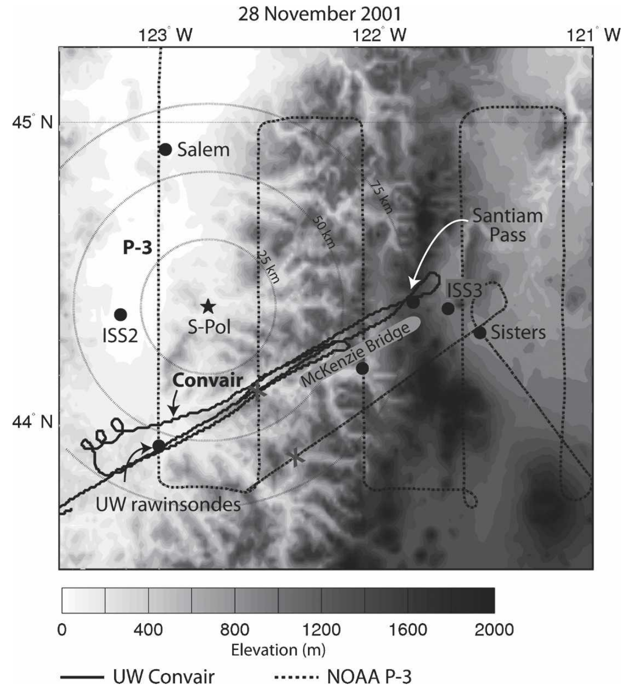

FIG. 2. The IMPROVE-2 study area showing locations of ground-based instrumentations and flight paths of the Convair (solid line) and P-3 (dashed line) aircraft on 28 Nov 2001. Upper-air soundings were taken at Salem and the UW rawinsonde site. The S-band vertical pointing radar was located at McKenzie Bridge. ISS2 and ISS3 measured surface conditions. The surface observations of ice particle types were made at Santiam Pass. Range rings centered at the S-Pol site are in increments of 25 km. The × symbols on the flight tracks indicate the reference point (horizontal range = 0 km) used in Figs. 8–10 and 12–14.

Heggli and Rauber 1988; Reynolds and Kuciauskas 1988). These storms often generate weak embedded convection aloft in association with the passage of an upper humidity front, leading to a significant warming (i.e., lowering) of the cloud top and weakening precipitation (stage 3). Heggli and Reynolds (1985) attributed this phenomenon to the circulation around the upper-tropospheric jet and the upper cold front. They also noted the presence of freezing drizzle at the ground level in association with the lowering of the cloud top. Additionally, the split front often generated low-level embedded convection within orographic clouds in association with potential instability, which developed after the surface cold-frontal passage (Heggli and Reynolds 1985), as well as shallow convective clouds forced primarily by local topographic lifting after the dissipation of the orographic clouds (stage 5).

An overview of the data used and the study area is given in section 2. Section 3 describes the 28 November 2001 storm using data collected in the postfrontal cloud (stage 5). The 13–14 December 2001 event is examined in section 4 with an emphasis on the intrafrontal and postfrontal periods (stages 3–5) followed by a discussion of the observed supercooled drizzle aloft (section 5). A summary and concluding remarks are given in section 6.

2. Study area and data

The IMPROVE-2 field study focused on a 55-km section of the Cascade Mountains in west-central Oregon (Fig. 2). The region is dominated by a near north–south-oriented mountain range having ridge heights typically 1.6 km above mean sea level (MSL).

The field data were collected with two instrumented aircraft [the University of Washington (UW) Convair-580 and the National Oceanic and Atmospheric Administration (NOAA) P-3], the NCAR S-band dual-polarimetric radar (S-Pol), an S-band vertical-pointing radar, upper-air soundings, and Integrated Surface Systems (ISS). Locations and descriptions of the instruments can be found in Stoelinga et al. (2003). Figure 2 shows the topographic map with the instruments discussed in this study and the flight tracks of the two aircraft during the 28 November 2001 operation.

The Convair was equipped with a Particle Measuring Systems, Inc. (PMS) forward scattering spectrometer probe (FSSP-100), which sampled concentrations of cloud droplets between 2 and 47 μm in diameter, and a PMS 2D-C probe for imaging particles between 25 and 800 μm. The P-3 carried a PMS King liquid water probe, PMS 2D-C grayscale probe (30–1920 μm), and PMS 2D-P probe (150–9600 μm). Liquid water contents in this study may be biased due to known tendencies of the King probes to underestimate the liquid water content associated with large drops (Strapp et al. 2000), and those of the FSSPs to interpret small quasi-spherical ice particles as droplets (Cober et al. 2001). When computing particle concentrations, the first size category of the FSSP data and particles smaller than 100 μm in diameter registered by the 2D-C probes were ignored because of known undercounting problems. Zero-area images that are produced when particles too small to shadow a pixel trigger the 2D probes, and artifacts from the particle breakups and splashes against the probe tips were also rejected. Drizzle and ice concentrations for flight segments of interests were computed based on the 100–300-μm size range and size categories >300 μm of the 2D-C data, respectively. These size ranges were selected because detailed visual inspections of the particle images from the flight segments studied showed that ice and snow particles were generally larger than 300 μm in diameter when they coexisted with drizzle.

The S-Pol radar, located upwind of the mountain range at an elevation of 475 m, performed range–height indicator (RHI) scans mostly in the eastern sectors and surveillance (SUR; full 360°) scans at 0.5° and 1.5° antenna elevation angles. The S-Pol radar had a dual-polarization capability.

Three-hourly upper-air sounding data were available from Salem, Oregon. Special rawinsondes were released by the University of Washington (UW) from approximately 55 km to the southwest of the S-Pol radar and underneath the general aircraft paths, providing upstream soundings. One-minute measurements of the surface conditions were collected at two ISS sites (ISS2 and ISS3). The S-band vertical pointing radar was located at McKenzie Bridge (elevation of 512 m). A surface observer stationed at Santiam Pass and Ray Benson Sno-Park (just south of Santiam Pass) provided field notes on crystal types, degree of riming, and aggregation. Santiam Pass and Ray Benson Sno-Park were above the melting layer during the study periods presented here.

3. 28 November 2001

a. *Synoptic and mesoscale conditions*

On 28 November 2001 a large low pressure system approached the northwest coast of the United States. The surface analysis for 1200 UTC (Fig. 3) shows the low pressure center as it approached Vancouver Island, British Columbia. With time, the low pressure center slowly moved eastward while the warm and cold fronts swept across the coastal region.

The passage of the warm front, which produced multiple freezing levels (0°C) over the study area, occurred shortly after 1100 UTC (Ikeda et al. 2005a), and the surface cold front propagated over the study area between 1800 and 1900 UTC. The period between the warm and the surface cold-frontal passages consisted of a deep stratiform cloud with cloud-top temperatures less than −60°C (Figs. 4a and 5a) producing light rain at the surface that intensified ahead of the surface cold front. The reflectivity cross section shows a pronounced bright band at 2.1 km MSL (1.6 km AGL; Fig. 4b). The post-cold-frontal clouds had a lower cloud deck in which convective elements were embedded near the top of the cloud deck (Fig. 4c). The satellite image at 1800 UTC shows that the post-cold-frontal cloud-top temperatures were between −10° and −20°C, with a typical value of −19°C (Figs. 5b,c). The rainfall gradually weakened and eventually became scattered as weak postfrontal convection moved over the study area (Figs. 4d and 5d).

The cold-frontal system was characterized with a surge of a relatively dry colder air above 5 km MSL that advanced ahead of the surface cold front (intrafrontal convection period) and strong onshore winds exceeding 40 m s^{-1} at low levels accompanying the surface cold front. These features resemble many Sierra Nevada storms of the split-front type (Reynolds and Kuciauskas 1988), and are clearly evident in the time–height cross section of the upper-air measurements from Salem (Fig. 6). In the figure, the times on the abscissas are relative to the passage of the cold front at a given location. For example, the surface cold-frontal passage occurred at 1830 UTC at the S-Pol site, and the aircraft measurements were collected approximately 3–5 h after

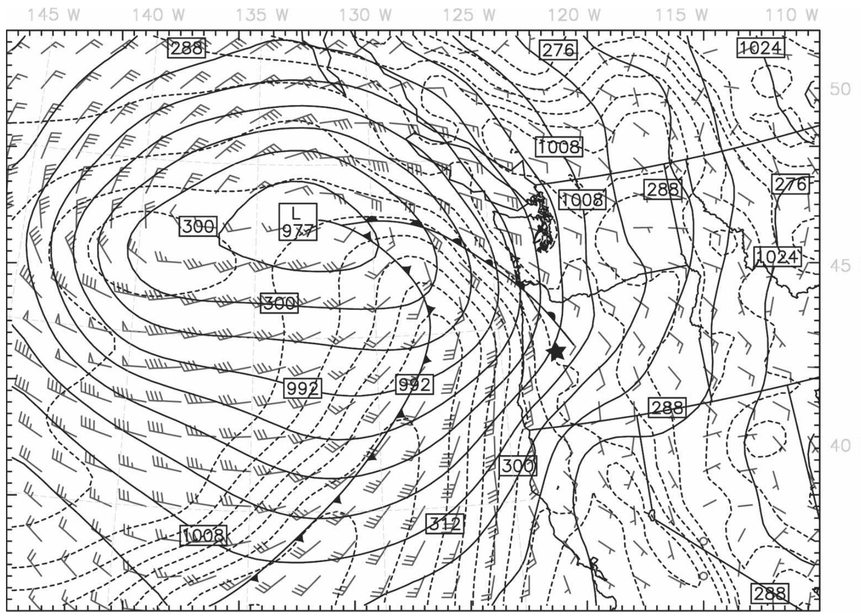

FIG. 3. Surface analysis at 1200 UTC 28 Nov 2001 showing mean sea level pressure (hPa) in solid lines, equivalent potential temperature (K) in dashed lines, and surface wind (full barb = 10 kt, where 1 kt = 0.514 m s^{-1}). The S-Pol site is indicated by a star.

the cold front had passed the location of the aircraft track (Fig. 2). The passage of the upper cold/humidity front was accompanied by a lowering of the cloud top that destabilized the region near the cloud top as observed in previous Sierra Nevada storms (e.g., Heggli and Reynolds 1985; Heggli and Rauber 1988). The convectively unstable layer is shown in Fig. 6a from hours 1 to 4 at heights between 4.5 and 5.5 km MSL (postfrontal convection period). Below this layer, a moist layer prevailed owing to the strong cross-barrier winds.

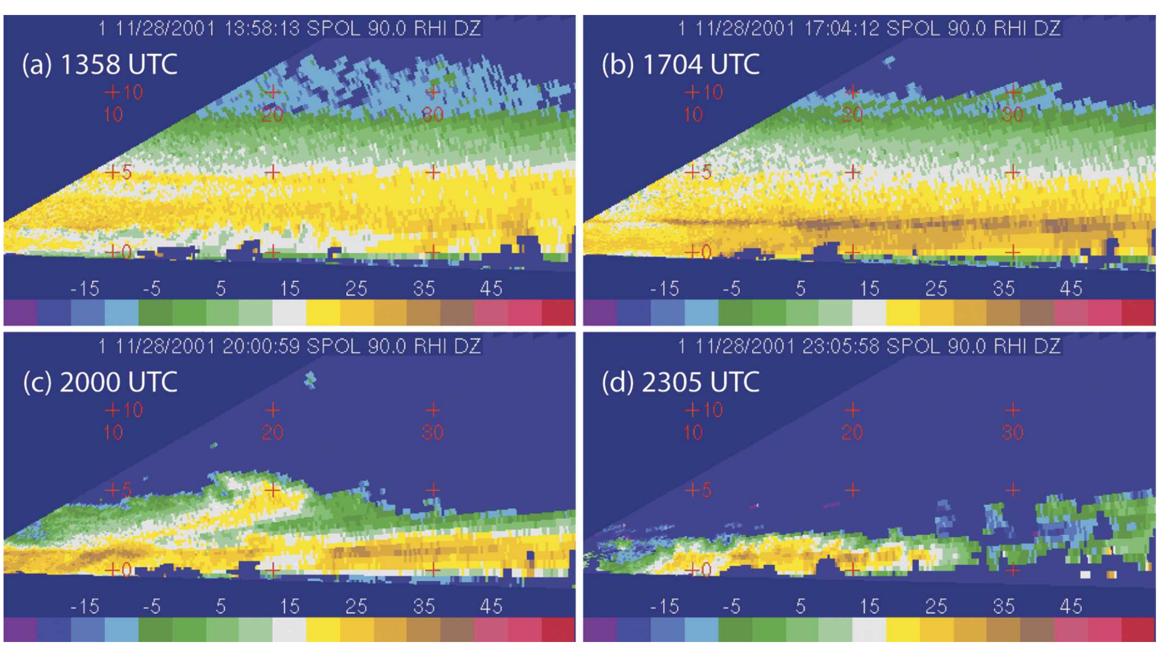

FIG. 4. Vertical cross sections of radar reflectivity (dBZ) for times indicated. Crosses indicate range (km) and height (km AGL) in increments of 10 and 5 km, respectively. The elevation at the radar site is 0.475 km MSL.

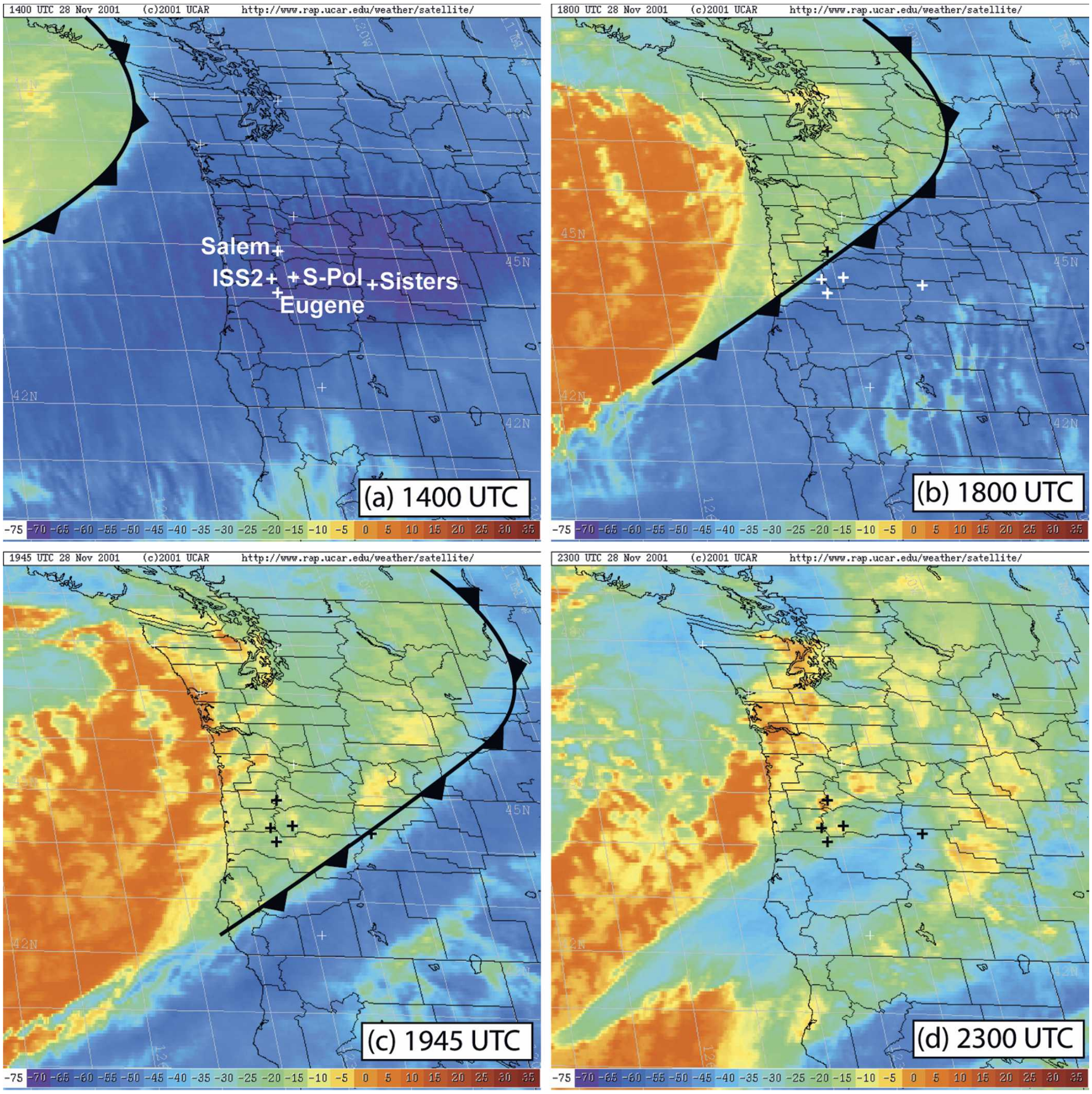

FIG. 5. Infrared satellite images taken at (a) 1400, (b) 1800, (c) 1945, and (d) 2300 UTC. Colors are temperatures in °C. The cold front is overlaid.

This storm was one of the strongest storms during the IMPROVE-2 project, with winds greater than two standard deviations over the 1976–92 climatology (Table 1). As a result, the Froude number was high, ranging between 1.5 and 2 below the typical mountain-top elevation (1.6 km MSL). This implies that the low-level air mass was lifted over the mountain barrier with little deflection, leading to the production of the orographic cloud that enveloped the mountain slopes well after the passage of the surface cold front.

The instability region associated with the passage of the upper cold/humidity front overturned and formed turrets (Figs. 4c and 7). These turrets generally advected with the mean flow across the study area at a speed of 30–35 m s^{-1} between 2000 and 2200 UTC based on a sequence of radar images. The turrets became less vigorous by 2040 UTC as the cloud top stabilized (Figs. 6 and 7), and the cloud layer became stratified after 2200 UTC. The average reflectivity field measured parallel to the Convair's southwest–northeast flight track between 2040 and 2200 UTC shows typical locations of generating cells (turrets) at a height of 5.2 km MSL and at horizontal distances 20, 35, and 68 km (Fig. 8a). These locations coincide with the local topographic ridges suggesting that vertical motions produced by these ridges may have contributed to the ini-

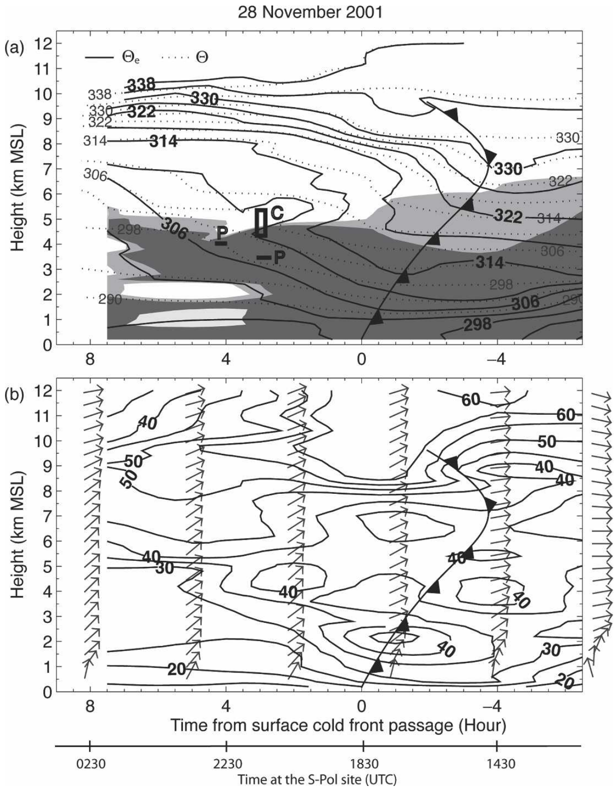

FIG. 6. Time–height cross sections of (a) equivalent potential temperature (solid; Θ_e in K), potential temperature (dashed; Θ in K), and relative humidity [≥80% (dark shaded), 70 ≤ RH < 80 (light shaded)]; and (b) horizontal wind speed (contours; m s^{-1}), and direction (arrows). The box in (a) encloses the time and flight altitudes of the Convair's flight operation (marked as C). The bold horizontal lines indicate the north–south (near hour 3) and the northeast–southwest (near hour 4) oriented flight legs of the P-3 (P). The data points are from the 3-hourly Salem soundings launched at times corresponding to the wind direction arrows. The cold front is overlaid.

tiation of the turrets. Numerical simulations of this storm system (not shown) have indicated that the strong cross-barrier flow could produce vertical velocities up to 2 m s^{-1} due to orographic uplift over local topographic ridges to deep levels when high Froude number air moves over such complex terrain in the absence of large-scale forcings. The Convair and P-3 observations collected during the instability period (near hour 3 in Fig. 6) are examined in the next section.

Approximately 3 h after the passage of the cold front at the surface (postfrontal convection period), the lower portion of the air mass became less stable (Fig. 6). Similar to the previous observations of the split-frontal systems, as this conditionally unstable air mass was forced up against the mountain slopes, weak embedded convection formed within the orographic cloud between 2200 and 2330 UTC. Based on a sequence of

TABLE 1. Average and standard deviation of wind speed at 850, 700, and 500 mb in the Oregon Cascade region based on synoptic data for the 1976–92 period.

	Avg (m s^{-1})	Std dev (m s^{-1})
850 mb	10.1	6.7
700 mb	14.1	7.5
500 mb	22.1	10.8

radar images, weak embedded convection appeared to strengthen while passing over individual ridges. The average reflectivity cross section shows a relatively stable echo top and the reflectivity increasing east of the 30-km range mark suggesting an orographic enhancement of the precipitation (Fig. 8b). The cloud-top temperature was −19°C. Observations made during the P-3's cross-barrier flight leg (Fig. 6) will be discussed in section 3c.

b. Aircraft observations associated with instability at cloud top

The Convair performed a southwest–northeast-oriented vertical stack (Fig. 2) through the region of instability near the cloud top (section 3a), and intercepted a portion of the cloud being sampled with RHI scans in the eastern quadrants of the S-Pol radar between 2145 and 2157 UTC. The aircraft closely followed the cloud top (4.6–5.4 km MSL) sampling both inside and outside of the generating cells (see Fig. 8 for the flight path). The temperature along the 5.4-km flight leg was approximately −19°C. At the 4.6-km level, the cloud was water saturated at a temperature of −14.5°C. The cloud water contents were typically between 0.05 and 0.2 g m^{-3} with a maximum value near 0.4 g m^{-3}.

The Convair passed through an area between two weak generating regions between 2152 and 2155 UTC at 4.6 km MSL, and subsequently a generating region from 2155 to 2157 UTC. Figures 9 and 10 show radar and aircraft observations corresponding to the two locations, respectively. The range–height cross sections (Figs. 9a and 10a) were produced using data from a set of RHIs between 2152 and 2200 UTC [through 81°–141° (azimuthal) at a 1° interval] while taking into account the northeastward movement of the generating cells at 30–35 m s^{-1} in order to match the radar measurements with the aircraft positions. The advection speeds of the precipitation features were determined from the sequence of RHI and SUR scans at a 10-min interval. Reflectivities greater than 24 dBZ near 2 km MSL are produced from melting snow.

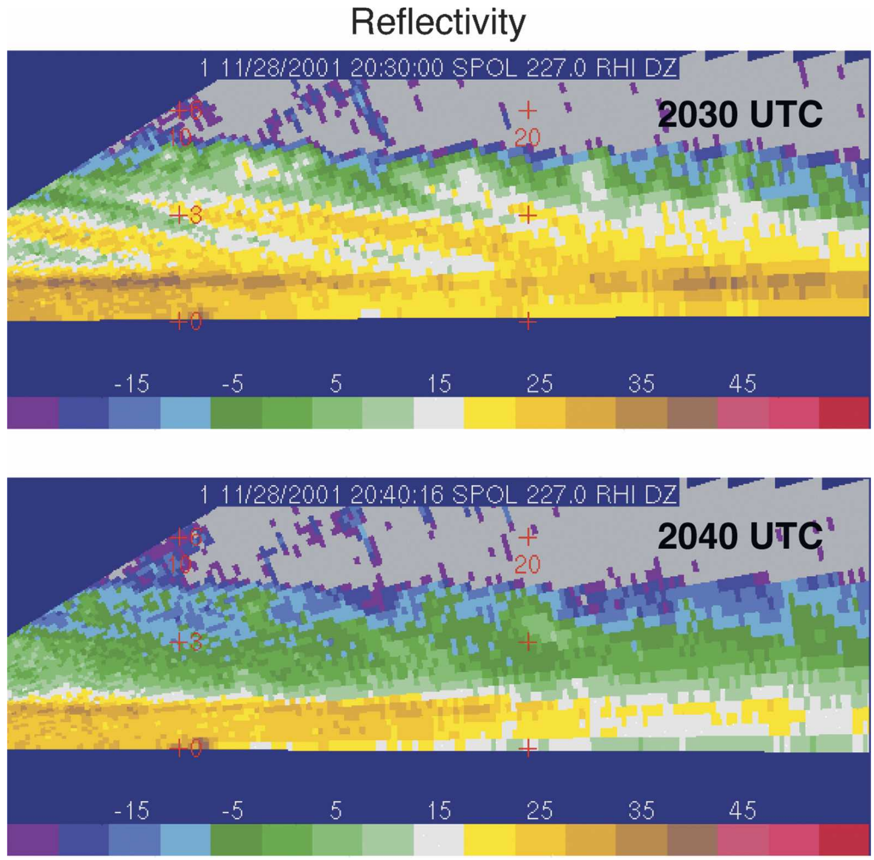

FIG. 7. Vertical cross sections of reflectivity (dBZ) for (top) 2030 UTC showing ice-generating cells and precipitation streaks, and (bottom) 2040 UTC showing the weaker generating cells aloft.

Visual inspections of the particle images from 2152 to 2155 UTC (outside the generating region) revealed that the particles smaller than 300 μm were supercooled drizzle drops, and larger particles were mostly planar ice crystals such as dendrites and stellar crystals (Figs. 9c,d). Evidence for the presence of drizzle include the roughly circular shape of the images and the presence of a Poisson spot—an optical effect generated by the 2D-C laser beam passing through the center of the drop and illuminating the detection sensor on the other side of the probe (Korolev et al. 1998). The concentration of ice crystals was 6 L^{-1} (>300 μm) while that of supercooled drizzle drops was 42 L^{-1} (100–300 μm). The light precipitation only produced reflectivity of ~5 dBZ. In contrast, the generating regions were dominated by a relatively high concentration (22 L^{-1}) of well-developed dendritic crystals, consistent with the higher reflectivity in this region (Fig. 10), and only a few drizzle drops were present. Flight observer notes of drizzle drops and the accretion of ice on the aircraft confirmed the presence of supercooled liquid drops during this flight leg. PIREPs from aircraft in the nearby area also indicated multiple incidences of icing.

Farther upstream of these locations (outside the radar coverage), supercooled drizzle was again observed in regions with ice concentration typically less than 1 L^{-1} and significant amounts of cloud liquid water (average of 0.1 g m^{-3}; a maximum of 0.4 g m^{-3}). A significant amount of glaze ice was accreted on the aircraft during this traverse (Fig. 11), and thus the aircraft exited out of the cloud to avoid further icing hazard.

The P-3 also encountered supercooled drizzle drops and reported icing within the same cloud during a north–south transect at 3.6 km MSL (Figs. 2 and 6). The cloud was saturated with respect to water at a temperature of -9°C at this flight level. The cloud water content outside the generating region was 0.13 g m^{-3} on average with a maximum of 0.2 g m^{-3}. As observed by the Convair, P-3 data collected with the 2D-C and 2D-P probes and an airborne Doppler radar indicated the presence of supercooled drizzle outside precipitation streaks. Zero-area images dominated the 2D-P dataset,

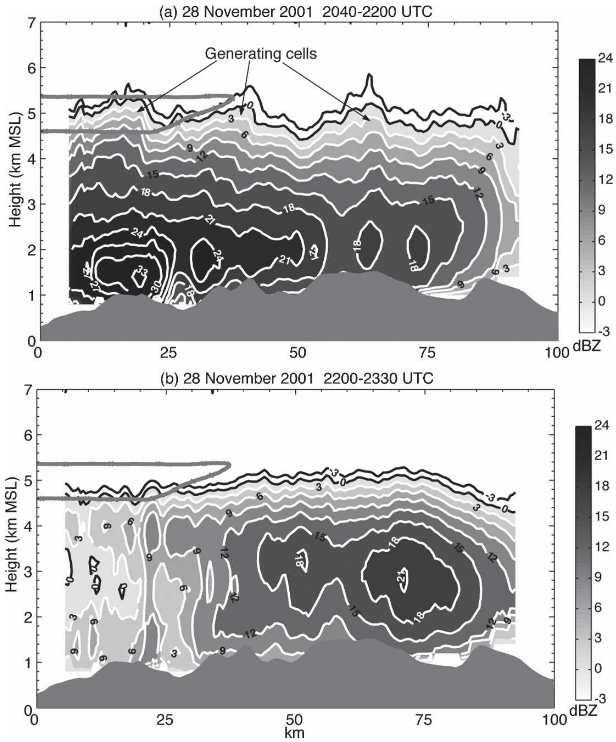

FIG. 8. Range–height cross sections along the Convair's northeast–southwest flight track (Fig. 2) showing the average reflectivity for (a) 2040–2200 and (b) 2200–2330 UTC. The bold gray line indicates the flight path. The terrain profile is also shown. The abscissa is the distance from $\times$ on the Convair flight path in Fig. 2 with positive toward the northeast. Large reflectivities below 2.5 km MSL in Fig. 8a are from the brightband effect.

which were identified as drizzle drops less than 200 μm in diameter in the 2D-C dataset. Few rimed ice particles were present, and the drizzle population dominated over ice (177 versus 1 L^{-1}).

The air mass in the current case was maritime with very low concentrations of cloud droplets (14–30 cm^{-3} based on the FSSP data and less than 30 cm^{-3} from the CCN counter at a supersaturation of 0.3%). In this condition, the predicted liquid water threshold value of 0.2 g kg^{-1} required to exceed before the onset of autoconversion to drizzle drops (Rasmussen et al. 2002) is close to the observed average liquid water content of 0.13 g kg^{-1}. Thus, given the fact that the ice concentrations were low and the cloud top was fairly warm, the presence of drizzle is entirely reasonable. The aircraft data revealed that small concentrations of ice crystals were not effective in depleting the liquid water with the consequent formation of drizzle outside of the generating regions while in the convective turrets significant ice concentrations suppressed the formation of drizzle-sized drops. An appreciable ascent in these turrets (greater than 0.5 m s^{-1} on average with a maximum of 1.2 m s^{-1}) measured by the P-3 partly explains the persistence of liquid water even inside the turrets. Since the temperatures were constant along the flight paths, the data suggested the importance of convective updraft–generated positive supersaturation fluctuation with respect to water for the generation of high concentration of ice crystals in these regions.

c. Aircraft observations associated with the low-level embedded convection

Radar data showed embedded convection at low levels within the well-developed orographic cloud starting at approximately 2200 UTC. This stage of the storm was sampled by the P-3 between 2300 and 2318 UTC along a cross-barrier flight path at 4.6 km MSL (Fig. 2). Temperature was $-13°C$ at this height (Fig. 12c). Measurements along the flight leg showed vertical velocity and cloud liquid water maxima that correlated well with the underlying topographic features (Figs. 12a,b,d). The maximum cloud water (0.19 g m^{-3}) and the maximum vertical motion (1.3 m s^{-1}) are collocated with the sharp incline leading to the peak of the barrier at a horizontal distance of 40 km. A subsidence of a comparable magnitude (-1.0 m s^{-1}), on the other hand, is found immediately downwind of the mountain peak, drying the air. Similarly, Garvert et al. (2005) found strong relations among the two variables and the underlying topography for a stronger storm on 13–14 December 2001 (section 4). Rasmussen et al. (1988) also identified similar correlation of updraft velocity with local ridges for a Sierra Nevada winter storm based on high-resolution model simulations. Given the observed maximum vertical motion of 1.3 m s^{-1}, an expected condensate supply rate is $\sim 1.0 \times 10^{-3}$ g m^{-3} s^{-1} (Rauber and Tokay 1991). If an average topographic slope is considered instead of the sharp incline, an average updraft of only 0.3–0.5 m s^{-1} is generated by the mean southwesterly flow, assuming no larger-scale motions (e.g., frontal lifting) thereby reducing the condensate supply rate by a factor of 2–3. These observations show the critical role that the local topography plays in locally enhancing the condensate supply rate over complex terrain.

The P-3 detected a significant amount of drizzle mixed with large aggregates, and significant icing over the mountain crest (Fig. 13). Observed ice particle concentrations were only 4 L^{-1}, which produced a depletion rate of 0.1–0.3 $\times 10^{-3}$ g m^{-3} s^{-1} from riming and 0.5–0.8 $\times 10^{-3}$ g m^{-3} s^{-1} from deposition in this portion of the cloud. However, the high vertical motion in this region created a large condensate supply that nearly balanced the depletion rates. In spite of the presence of

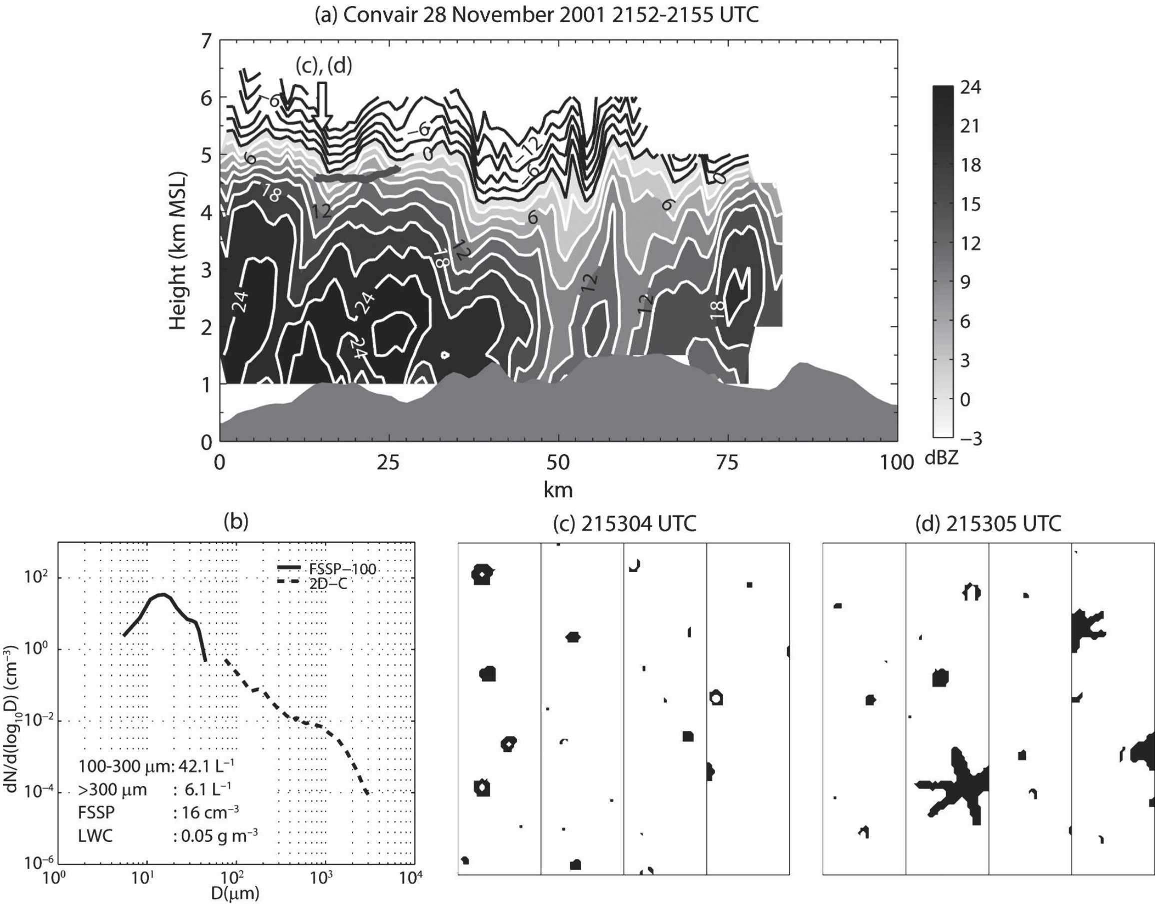

FIG. 9. (a) Reflectivity cross section the same as in Fig. 8, but reconstructed from radar data corresponding to the Convair's drizzle observations between 2152 and 2155 UTC (bold line at ~4.6 km MSL). (b) Average particle size distribution of the time segment based on the FSSP (solid) and 2D-C (dashed) data. Average drizzle (100–300 μm), ice (>300 μm), and FSSP concentrations, as well as cloud liquid water content (LWC) are indicated. (c), (d) Sample 2D-C images. The arrow in (a) indicates the along-flight leg location where the sample images were collected. The width of a 2D-C strip is 0.8 mm.

drizzle drops as large as 272 L^{-1} in concentration, the radar return from the large aggregates dominated over the small drizzle drops, yielding a relatively large reflectivity of ~15–20 dBZ. These observations show that hazardous amounts of supercooled drizzle can exist even when the reflectivity is relatively high if the condensate supply rate is higher than the depletion rate. The field notes from the crystal observers at Santiam Pass (Fig. 2) indicated graupel and heavily rimed ice crystals, which confirm the presence of mixed-phase conditions aloft. In contrast, in a region upwind of the mountain crest, rimed snow aggregates were the dominant particle type (Figs. 14b,c). This area was also over a local topographic ridge, but there was no significant vertical motion and liquid water.

4. 13–14 December 2001

A stronger, deeper storm system occurred on 13–14 December 2001. Similar to the 28 November 2001 case, the storm structure shared similarities with the split-front model. This storm has been well documented by Woods et al. (2005) and Garvert et al. (2005). In this section, we focus on supercooled drizzle episodes that occurred during the intrafrontal convection and postfrontal stages of this system. Figure 15 shows the flight tracks examined herein.

a. Synoptic and mesoscale conditions

The storm was dominated by an intense upper-level baroclinic zone. A surface front extended to a height of 3.5 km MSL, and an upper cold front was present above this level (Fig. 16). The passage of the upper cold front occurred between 2300 UTC 13 December 2001 and 0200 UTC 14 December 2001. An elevated precipitation shield with cloud-top temperatures less than −40°C was present ahead of the upper cold front above a low-level orographic cloud layer. At 0018 UTC, an elevated melting layer was centered at 1.6 km MSL

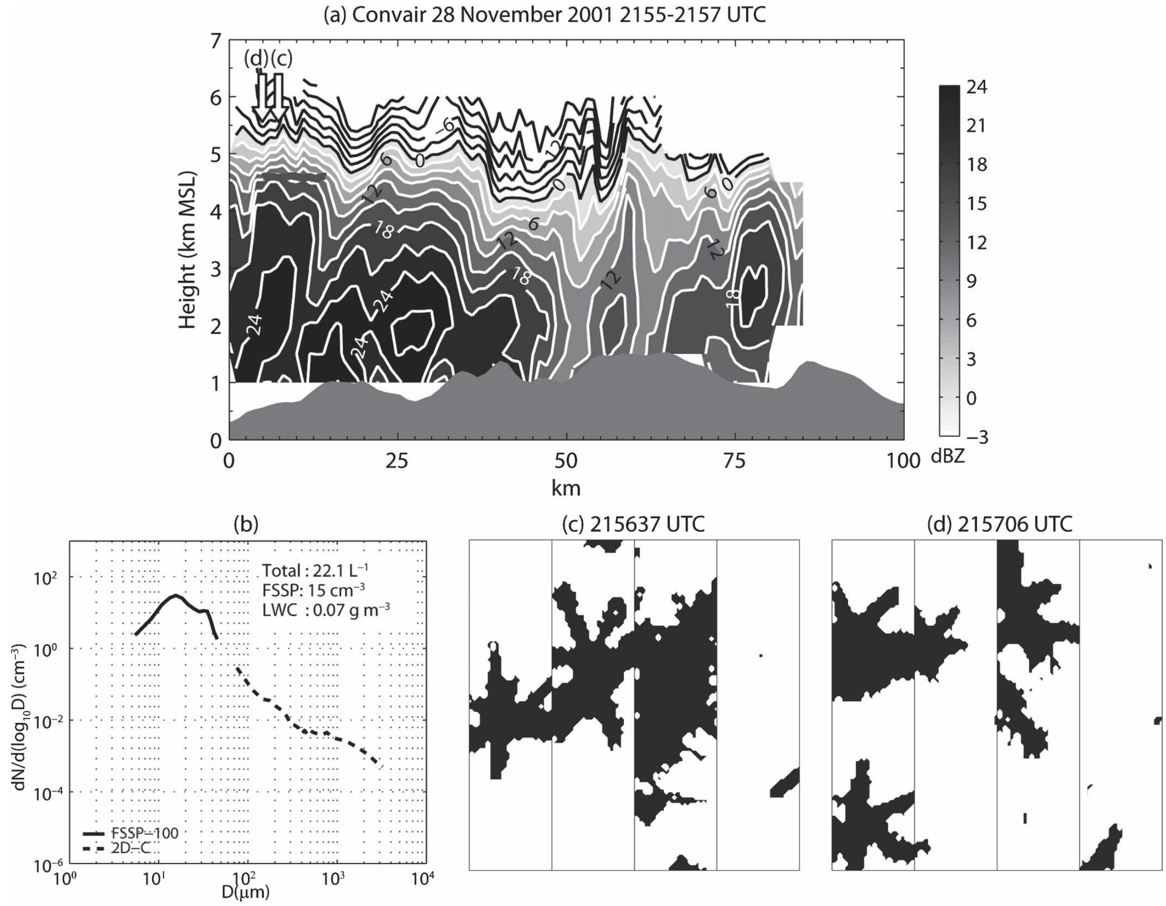

FIG. 10. Same as in Fig. 9, but for the Convair's ice particle observations between 2155 and 2157 UTC. (b) The total particle concentration is computed from particles larger than 100 μm in diameter.

($\sim$1.1 km AGL; Fig. 17a). The P-3 flew a northeast–southwest-oriented flight leg between 0105 and 0125 UTC within the precipitation shield (Figs. 15–16). Similar to the previous storm, strong low-level southwesterly flow up to 40 m s^{-1}, which was over two standard deviations higher than climatology (Table 1), accompanied the front.

An interesting feature developed within the cloud system during the onset of the intrafrontal convection period. Drying in the mid levels following the passage of the upper cold front left two cloud layers; a higher 1-km-thick layer centered at 5.5 km MSL (5.0 km AGL) and a shallow, less than 2-km-thick orographic cloud just above the mountain surface (Fig. 17b; indicated by a double-sided arrow). The orographic cloud had a relatively warm cloud top with temperatures between $-15°$ and $-12°$C, and produced light precipitation with weak reflectivity (hereafter the weak echo region). The weak echo region first entered the radar coverage domain near 0019 UTC (Fig. 17a; northwestern quadrant) and propagated southwestward. The deep precipitation ahead of the upper cold front was on the eastern side while that of the intrafrontal period was on the western side of the weak echo region. Key radar features of the weak echo region (Fig. 17b) are the absence of a reflectivity bright band and a shallow precipitation layer. These features have been shown by Neiman et al. (2005) to be consistent with the presence of drizzle produced mostly from a collision–coalescence process in presence of strong low-level upslope flow in the coastal regions of southern Oregon and northern California while deeper radar echoes with a prominent bright band were shown to be indications of hydrometeor growth dominated by ice processes. The P-3 sampled the weak echo region during its north–south transect between 0148 and 0210 UTC (Fig. 15). The Convair made multiple penetrations through the area while performing a southwest–northeast-oriented vertical stack (Fig. 15). Supercooled drizzle was observed in this region and will be discussed in later sections.

Once the weak echo region exited out of the radar domain, moisture returned in the 2–5 km MSL layer

FIG. 11. A photograph of glaze ice on the Convair taken after experiencing aircraft icing between 2152 and 2207 UTC.

(Fig. 16a). The orographic cloud layer deepened over the mountain slopes (Fig. 17c), and broad rainbands formed in association with strong embedded convection.

In the subsequent period (surface-frontal precipitation period), narrow well-defined rainbands associated with the surface cold front propagated across the radar coverage area. Figure 17c shows the surface-frontal rainband approaching the radar site from the west-northwest. The passage of the surface front at the radar site was at 0330 UTC, and the surface-frontal precipitation period lasted less than 1 h.

Following the passages of the surface rainbands, much weaker and shallower postfrontal convection became dominant (Fig. 17d; postfrontal convection period). The convection was embedded in orographic clouds over the mountain slopes that were also shallower and less significant by this time. Cloud-top temperatures varied between −17° and −28°C depending on the penetration height of the turrets. Winds behind the surface cold front were from the southwest at heights greater than 3 km MSL (Fig. 16b). At low levels, they were from the west-northwest and west, nearly perpendicular to the general orientation of the mountain crest and were favorable for moisture advection into the study area at low levels. The air mass was maritime in nature, having CCN concentration of 15–30

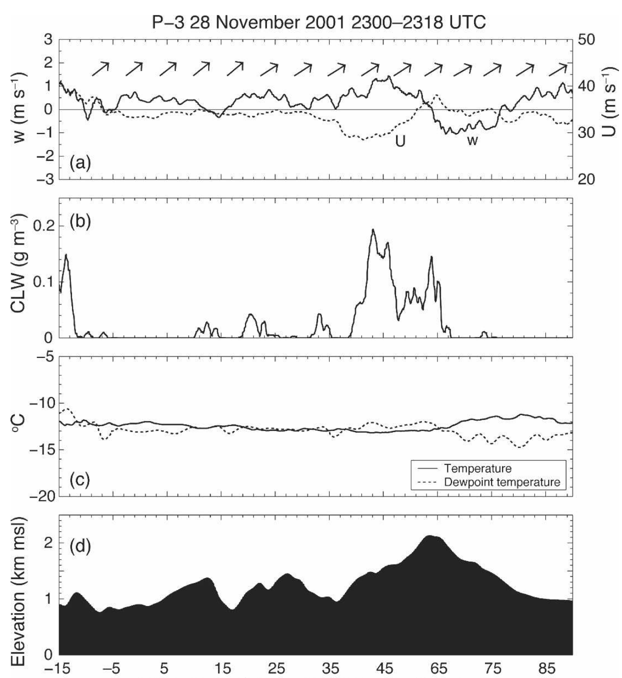

FIG. 12. Measurements of (a) vertical (solid; w) and horizontal (dashed; U) velocities, and horizontal wind direction (arrows); (b) King liquid water content (CLW); (c) temperature and dewpoint temperature; and (d) terrain profile along the P-3's northeast–southwest flight track between 2300 and 2318 UTC. The × on the P-3 flight path in Fig. 2 corresponds to 0 km.

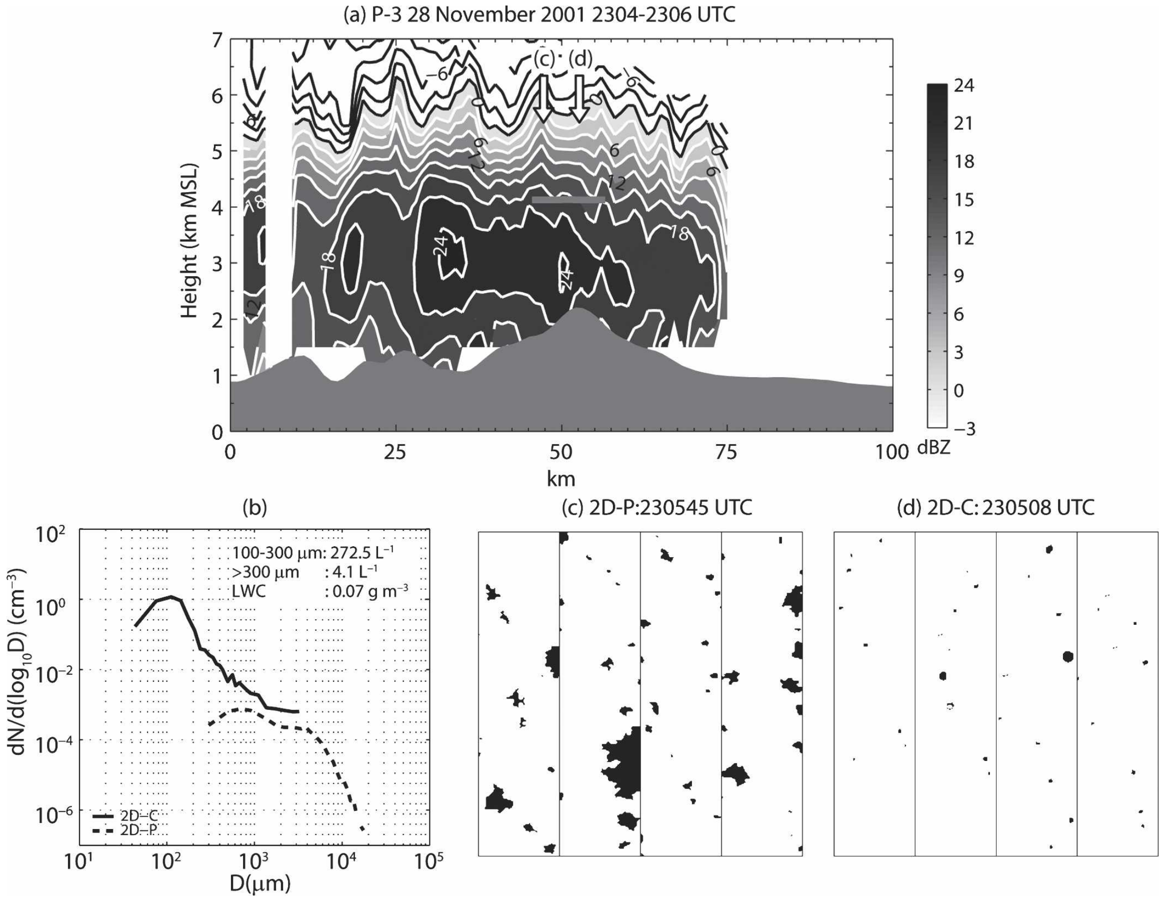

FIG. 13. (a) Reflectivity cross section corresponding with the P-3's observations between 2304 and 2306 UTC during its cross-barrier northeast–southwest flight. Radar beams were partially blocked between 5 and 10 km. (b) Average particle size distribution of the flight segment based on the 2D-C (solid) and 2D-P (dashed) data. The drizzle droplet (100–300 μm) and ice particle (>300 μm) concentrations from the 2D-C measurements, and cloud LWC are indicated. (c), (d) Sample 2D-P and 2D-C images collected at the locations (along the flight path) indicated with the two arrows in (a), respectively. The width of a 2D-P strip is 4 mm and that of a 2D-C strip is 1.6 mm.

cm^{-3} at supersaturations of 0.3%–0.7% and 48 cm^{-3} at 0.97%. The Convair's measurements during the postfrontal convective period are discussed in a later section.

b. *Observations in the precipitation shield ahead of the upper cold front*

The P-3's cross-barrier leg between 0105 and 0113 UTC sampled the deep cloud associated with the precipitation shield. As observed during the previous case, a significant upward–downward motion couplet was present over the mountain crest. The maximum updraft on the windward side of the crest was 1.5 m s^{-1}, and the corresponding downdraft on the lee side was -2.0 m s^{-1} at the flight altitude of 4 km MSL ($T = -12°$C; Fig. 18). Associated with the large ascending motion was a maximum cloud liquid water of 0.2 g m^{-3}.

Particle images through this portion of the cloud were mostly aggregates. The ice concentration between the 45- and 50-km range, in a region of high liquid water content, was 4–5 L^{-1} on average. Only a small amount of supercooled drizzle was present ($\sim$7 L^{-1}). Zero-area images from the 2D-C probe were evident, and many aggregates showed evidence of riming, confirming the presence of significant cloud water aloft. However, because of the presence of the cold altostratus deck, ice crystals were readily generated, and acted as natural seeding agents as they fell into the moist orographic cloud promoting further growth through aggregation as documented by Woods et al. (2005) for the current storm and by Marwitz (1987) in a deep orographic storm over the Sierra Nevada (cloud-top temperature of about $-25°$C). Thus, in this case, the enhanced condensate supply ($\sim 1.0 \times 10^{-3}$ g m^{-3} s^{-1}) associated with

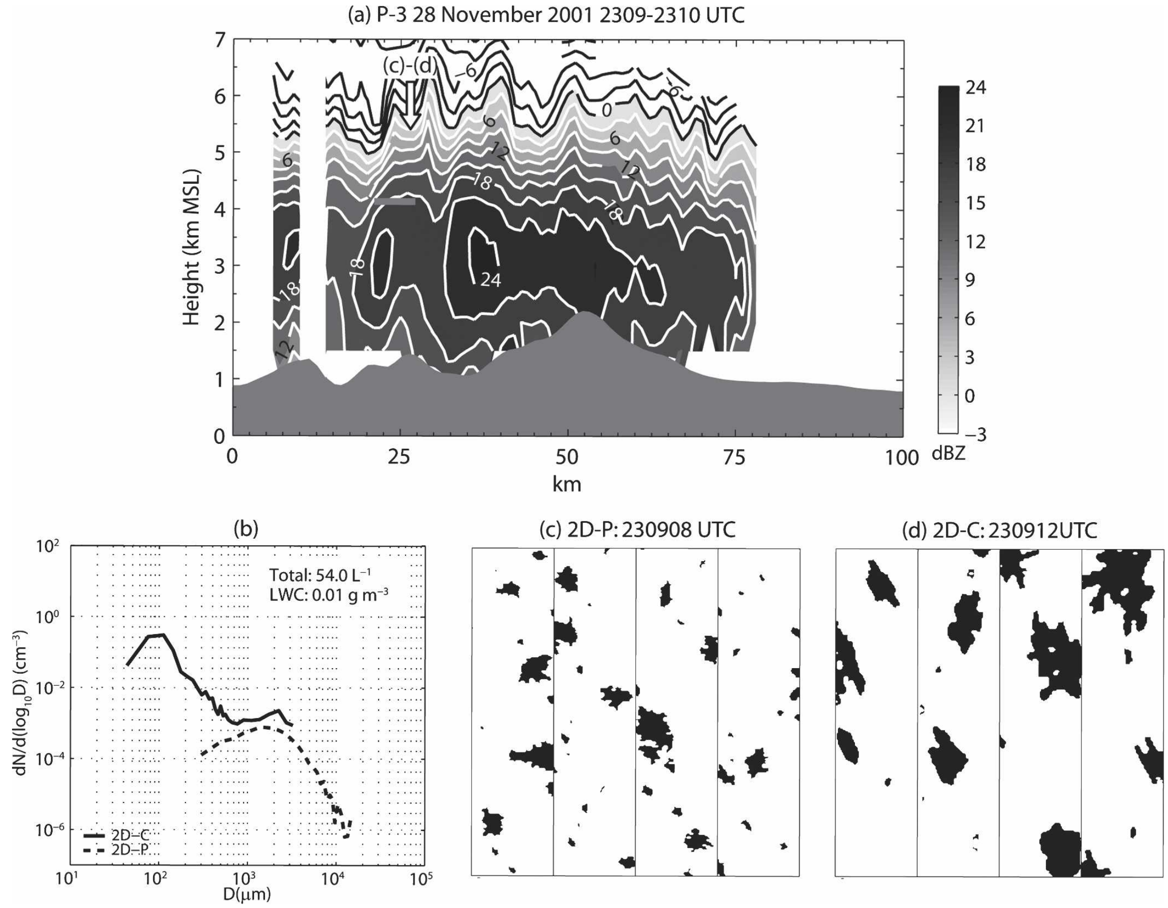

FIG. 14. Same as in Fig. 13, but for snow observations between 2309 and 2310 UTC. (b)The total 2D-C particle concentration (>100 μm) and cloud LWC are indicated.

the large vertical lift was not enough to overcome the high depletion rate (3.0×10^{-3} g m^{-3} s^{-1}) of the supercooled liquid water due to riming by the observed concentration of ice crystals.

c. *Observations of freezing drizzle in the weak echo region (~0200 UTC)*

This section presents aircraft observations from the period during which the weak echo region discussed in section 4a was over the windward slopes. Figure 19 displays cross sections of reflectivity at five different times along the Convair flight path (Fig. 15). The 0°C level was at approximately 1.9 km MSL. (The radar echoes below 1.6 km MSL are masked in Fig. 19.) The wind veered from southerly below 1 km MSL to southwesterly above 1.8 km MSL. Thus, the cross section is nearly parallel to the mid- and upper-level airflow. The cross sections were reconstructed from RHIs taken every 10 min between 60° and 121° azimuthal directions. The bold arrow through Figs. 19a–e connects the weak echo region as it moved from left to right in the cross section. The horizontal lines overlaid on each frame are segments of the Convair flight path that intersected the cross section near the radar beams (generally within a time offset less than 3 min) and within which area the particle habits did not change significantly. The hydrometeor images on the right-hand side are those sampled during the time segments. Particle size distributions corresponding to the flight segments in Figs. 19a,c–e are shown in Fig. 20.

Figure 19a shows the elevated precipitation shield (altostratus cloud) at heights greater than 5 km MSL. This layer contained ice generating regions responsible for seeding the lower orographic cloud (see section 4b). Ice crystals produced in cell A slowly descended while drifting toward the right (Figs. 19a,b). Subsequently, cell B entered the cross section, eventually becoming indiscernible as it merged with the orographic cloud just downwind of the mountain crest (Figs. 19b–d). The elevated precipitation shield moved off after ~0231

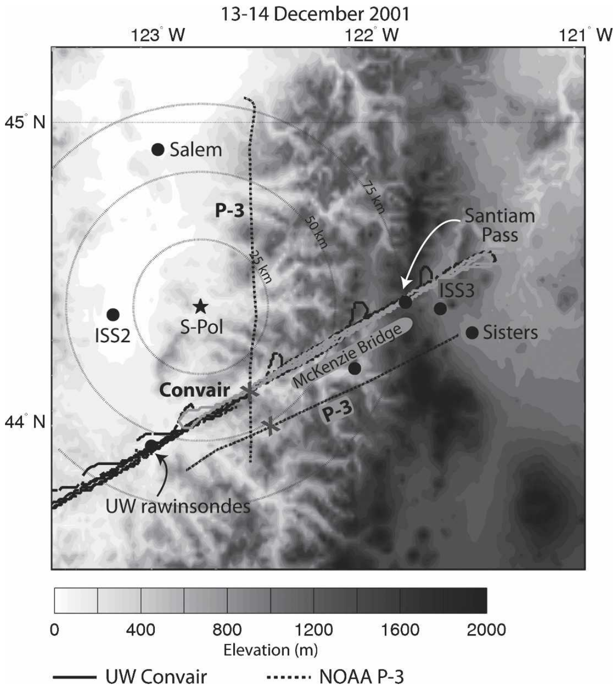

FIG. 15. Same as in Fig. 2, but with flight tracks on 13–14 Dec 2001. Dashed lines are for the P-3 flight track during 0105–0125 UTC (northeast–southwest), and 0148–0210 UTC (north–south). The thick black (gray) line is for the Convair flight track during the intrafrontal (postfrontal) period on 13–14 Dec 2001. The × symbols on the flight tracks are reference points for Figs. 18, 19, and 23–25.

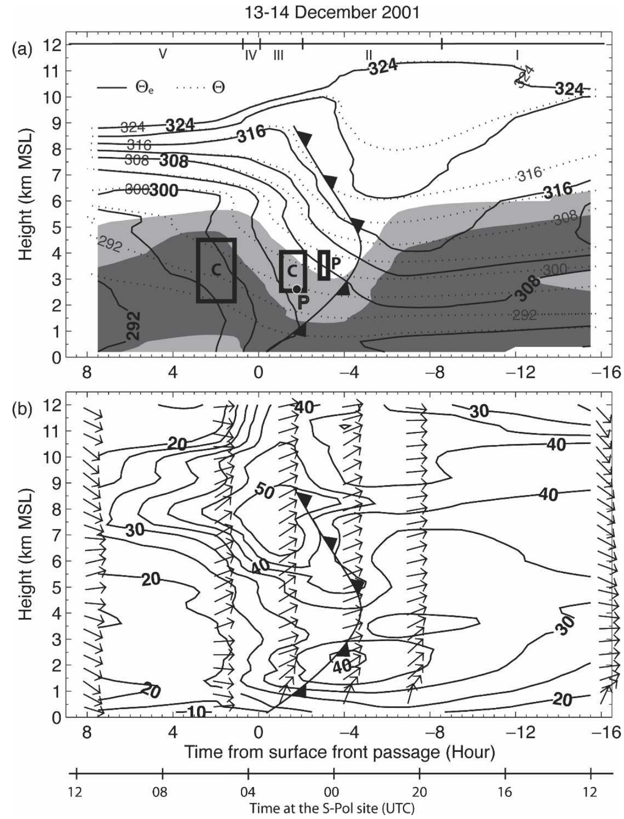

FIG. 16. Same as in Fig. 6, but for the 13–14 Dec 2001 storm. The box marked P encloses the P-3's flight time and altitudes during its northeast–southwest flight leg, and the dot marked P corresponds with the P-3's drizzle observations. The boxes marked C are for the Convair's northeast–southwest flight legs during the intrafrontal and postfrontal periods (Fig. 15). Indicated in (a) at the top are five stages of the storm system defined in Woods et al. (2005): 1) prefrontal showers, 2) upper cold-frontal rainband, 3) intrafrontal convection, 4) surface-frontal precipitation, and 5) postfrontal convection (section 1).

UTC and was followed by the weak echo region. The weak echo region first appears on the left-most edge of the reflectivity field in Fig. 19a, and it is more clearly shown below cell B in Fig. 19b (reflectivity <0 dBZ). This feature moved over the mountain slope reaching the mountain crest by 0231 UTC (Fig. 19d). Afterward, the additional intrafrontal precipitation moved into the region (Figs. 19d,e).

The Convair first entered the weak reflectivity region at an altitude of 4 km MSL (−13.6°C; 0200–0204 UTC). An abundance of supercooled drizzle drops was observed within this region (Fig. 19a, right column). Ice particles and aggregates were essentially absent. The aircraft again encountered the weak reflectivity region at a lower altitude (3.5 km MSL, −11.3°C, 0230:05–0232:53 UTC). An abrupt change in particle types detected with the 2D-C—from mostly needles and aggregates of needles in the convective region (associated with higher reflectivity) to drizzle drops in the weak echo region—accompanied this penetration (Fig. 19c). Flight observer notes indicated the presence of supercooled drizzle drops, a thinning of the cloud layer aloft, and a buildup of icing on the aircraft for brief moments during these two penetrations. Furthermore, freezing drizzle/frozen drops were reported by the crystal observers at Ray Benson Sno-Park near the time of the passage of the weak echo region (cf. Fig. 16 in Woods et al. 2005), and PIREPs indicated that aircraft icing occurred in the nearby regions possibly associated with the same cloud feature. The P-3's north–south flight leg at 2.6 km MSL (−3.2°C; Fig. 15) intersected the weak echo region between 0201 and 0205 UTC and encountered supercooled drizzle drops, confirming the Convair observations. The radar reflectivity cross section along the P-3 flight track (Fig. 21a) shows a shallow precipitation layer below 3 km MSL and a thin layer of altostratus cloud layer aloft as in Fig. 19. Essentially no particles were detected with the 2D-P (Fig. 21b), and the cloud liquid water content was on the order of 0.56 g m^{-3}.

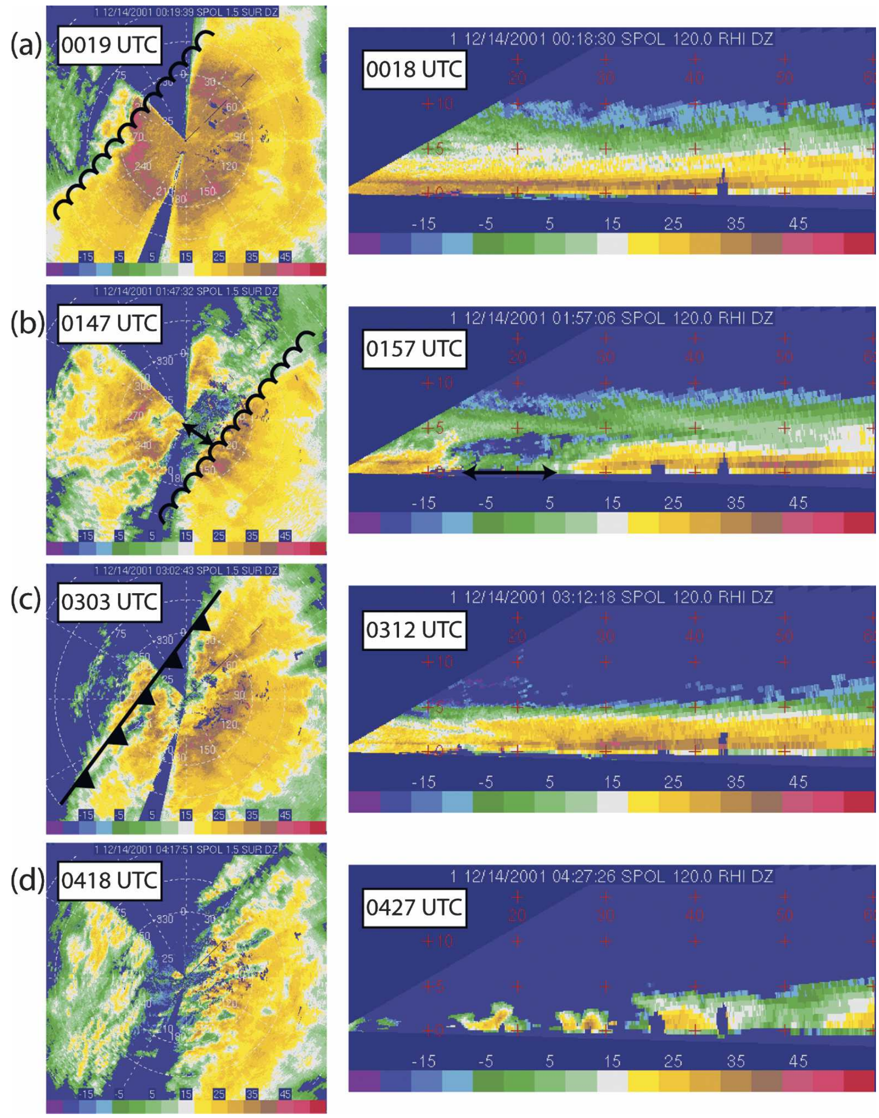

FIG. 17. (a)–(d) Radar reflectivity (SUR scans at the 1.5° antenna elevation on the left and RHI scans through an azimuth angle of 120° on the right) for times indicated. The cusped line in (a) and (b) denotes the leading edge of the weak echo region [also marked with a double-sided arrow in (b); see text]. The surface cold front is overlaid in (c). Range rings on the SUR images are in increments of 25 km. Crosses in the RHI images indicate range (km) and height (km AGL) in increments of 10 and 5 km, respectively.

After exiting the weak echo region the Convair entered a portion of deep cloud associated with the precipitation shield and found a mixture of supercooled drizzle drops and aggregates of dendrites (Fig. 19d; −11.6°C; 0232–0235 UTC). The last penetration through the weak echo region was at 3.0 km MSL (−8.9°C, 0241:15–0242:00 UTC; Fig. 19e). By this time, the weak echo region had passed over the mountain peak. The cloud inside this region was mixed phase, but it still contained a significant number of drizzle drops mixed with heavily rimed ice crystals, and graupel. Note that the ground targets and power attenuation impact the reflectivity measurements at this distance. Inside the convective intrafrontal cloud upstream of the mountain crest, aggregates of dendrites were the dominant particle type, consistent with the higher reflectivity found there.

In the weak echo region, supercooled drizzle drops were dominant in regions of cloud liquid water on the order of 0.14 g m^{-3}, ice concentrations ranging from 0.3

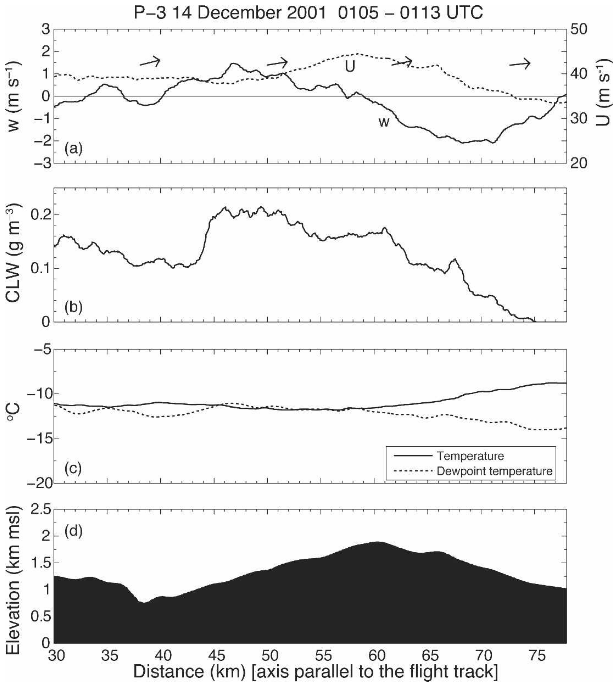

FIG. 18. Same as in Fig. 12, but for the P-3's flight between 0105 and 0113 UTC on 14 Dec 2001.

and 1.2 L^{-1}, and low cloud drop concentrations between 28 and 50 cm^{-3} (Figs. 20a,c). In contrast, liquid water contents were low in the lee of the barrier, where downdrafts occurred (Fig. 20e), and in the region of high ice crystal concentrations associated with the deeper cloud in which the seeder-feeder process was active (Fig. 20d). These observations indicate that the absence of an upper seeder cloud clearly played an important role in drizzle formation within the weak echo region having sufficient updrafts. The bimodal cloud droplet size distribution in Fig. 20a and to some degree in Fig. 20c also suggests that the onset of the collision–coalescence process occurred rapidly due to the presence of relatively large cloud drops in this clean air mass. In contrast, active ice nucleation and seeder-feeder processes occurring in the deeper cloud ahead of the weak echo regions and in convective intrafrontal precipitation produced ice crystals that depleted supercooled liquid water and liquid droplets at low levels, consistent with earlier observations by the P-3 (section 4b) and as documented by Woods et al. (2005).

d. The postfrontal shallow precipitation

The Convair also encountered supercooled drizzle in selective regions of the postfrontal clouds (Fig. 16; stage 5). Early precipitation during this storm stage was convective (0530–0620 UTC in Fig. 22 or 1–2.3 h after the passage of the surface cold front). The convective cores reached between 4 and 5 km MSL according to measurements with the vertical-pointing radar (Fig. 22) and the S-Pol radar (Fig. 23), in which layer the temperature varied between −17° and −24°C. The weak convection traveled with the west-northwesterly low-level winds. As the convection approached the mountain slopes, it became embedded with the preexisting orographic cloud. The orographic cloud layer was shallow with tops less than 3 km MSL by this time. Later, a stratiform cloud deck formed over the weakening shallow surface convection and deepened with time over the mountain slopes (after 0620 UTC in Fig. 22). The evolution of the clouds was generally similar to that observed in the 28 November storm except that that the low-level moisture layer was colder and shallower on 14 December. At the ground crystal observation site, graupel particles were mostly observed in the early period and aggregates of dendrites and needles were dominant in the latter period (Woods et al. 2005).

The Convair sampled regions of the weak convective clouds between 0541 and 0558 UTC during a southwestward cross-barrier flight leg (Figs. 15 and 23). Temperatures at the flight level between 3.8 and 4.0 km MSL were −19°C on average. Penetrations through convective cores showed the peak liquid water contents, on the order of 0.1 g m^{-3}, collocated with the regions of high particle concentrations (Fig. 24a) and high reflectivity (e.g., Fig. 23a) indicating that liquid water was carried upward by convective updrafts. The interior of the convective core was mixed phase with rimed ice crystals, graupel particles, and a few supercooled drops (Fig. 23c).

More significant observations of supercooled drizzle drops were made in between the convective cores where the shallow orographic cloud persisted, and at the top of the stratiform cloud layer, which developed in the latter half of the postfrontal period. Figure 25a provides a typical example of this behavior based on radar and aircraft data between 0620:30 and 0623:40 UTC. Temperatures at the flight level were −18°C. The echoes beyond 55 km correspond to weak convective cells that were moving out of the study area. The nearer (<50 km) echoes were from the stratiform cloud that formed after the period of shallow convection. Drizzle drops less than 300 μm in diameter are evident (Figs. 25c,d). Snow particles greater than 300 μm were generally absent (Fig. 25b), resulting in a reflectivity of 0 dBZ or less. The FSSP spectra were bimodal (Fig. 25b) similar to those observed in the weak echo region. In contrast to the liquid water trace from the earlier

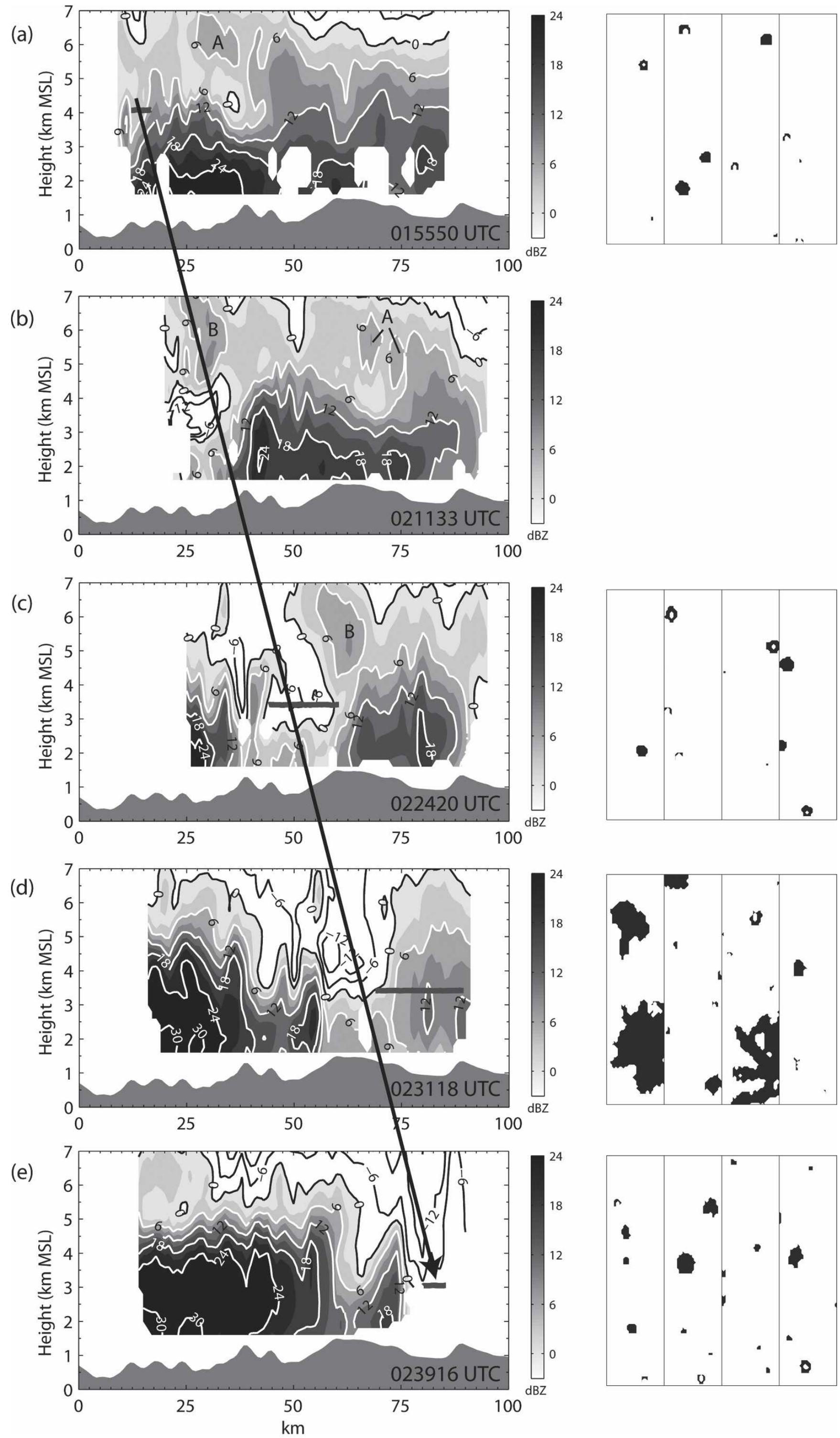

FIG. 19. (a)–(e) Reconstructed RHIs along the Convair's flight track (Fig. 15) showing the radar reflectivity. The abscissa is the distance from × in Fig. 15 with positive toward the northeast. Solid horizontal lines are segments of the flight corresponding to the reflectivity cross sections with a minimal time lag. The time indicated on each frame is associated with the northeastmost RHI scan. (right column) The 2D-C images show example hydrometeors observed along the flight segments. The radar bright band is centered at ~2 km MSL.

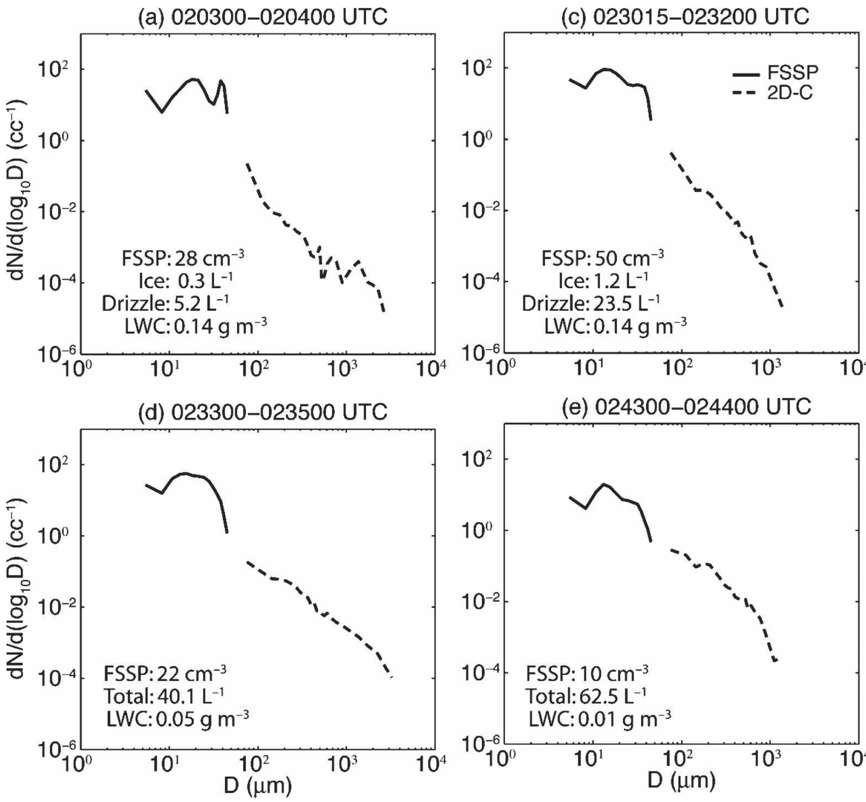

FIG. 20. Average particle size distributions for the flight segments corresponding to Figs. 19a,c–e. (a), (c) Ice particle (>300 μm), drizzle (100–300 μm), and FSSP concentrations are indicated for the time segments of drizzle observations. (d), (e) Total particle (>100 μm) concentrations are indicated.

traverse, the liquid water was continuously present at the flight altitude (3.6 km MSL) during the traverse near the top of the stratiform cloud layer (Fig. 24b). It suggests that the liquid water developed in response to a gradual lifting of low-level air mass over the mountain slopes. Enhanced liquid water was measured above the local topographic ridges similar to what was observed on 28 November.

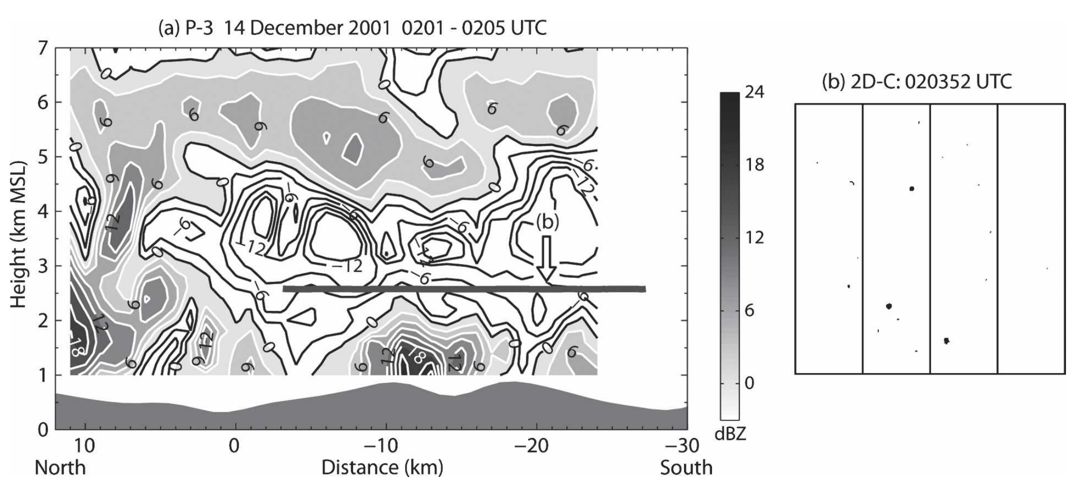

FIG. 21. (a) Reconstructed RHI corresponding to the P-3's north–south flight track between 0201 and 0205 UTC (bold horizontal line) during a freezing drizzle observation. The abscissa is the distance in the north–south direction from the latitude at the S-Pol radar site. (b) A sample 2D-C image at the location indicated with an arrow in (a). Essentially no particles were in the 2D-P probe size range during this time segment.

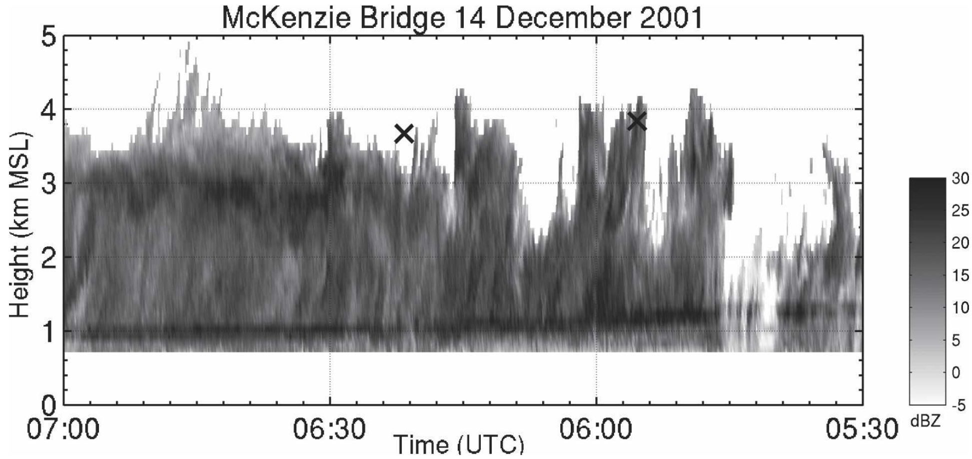

FIG. 22. The reflectivity measurements with the S-band vertical pointing radar at McKenzie Bridge (Fig. 15). The Convair passed 15.6 km directly north of the vertical-pointing radar site at 0555 and 0621 UTC (× symbols).

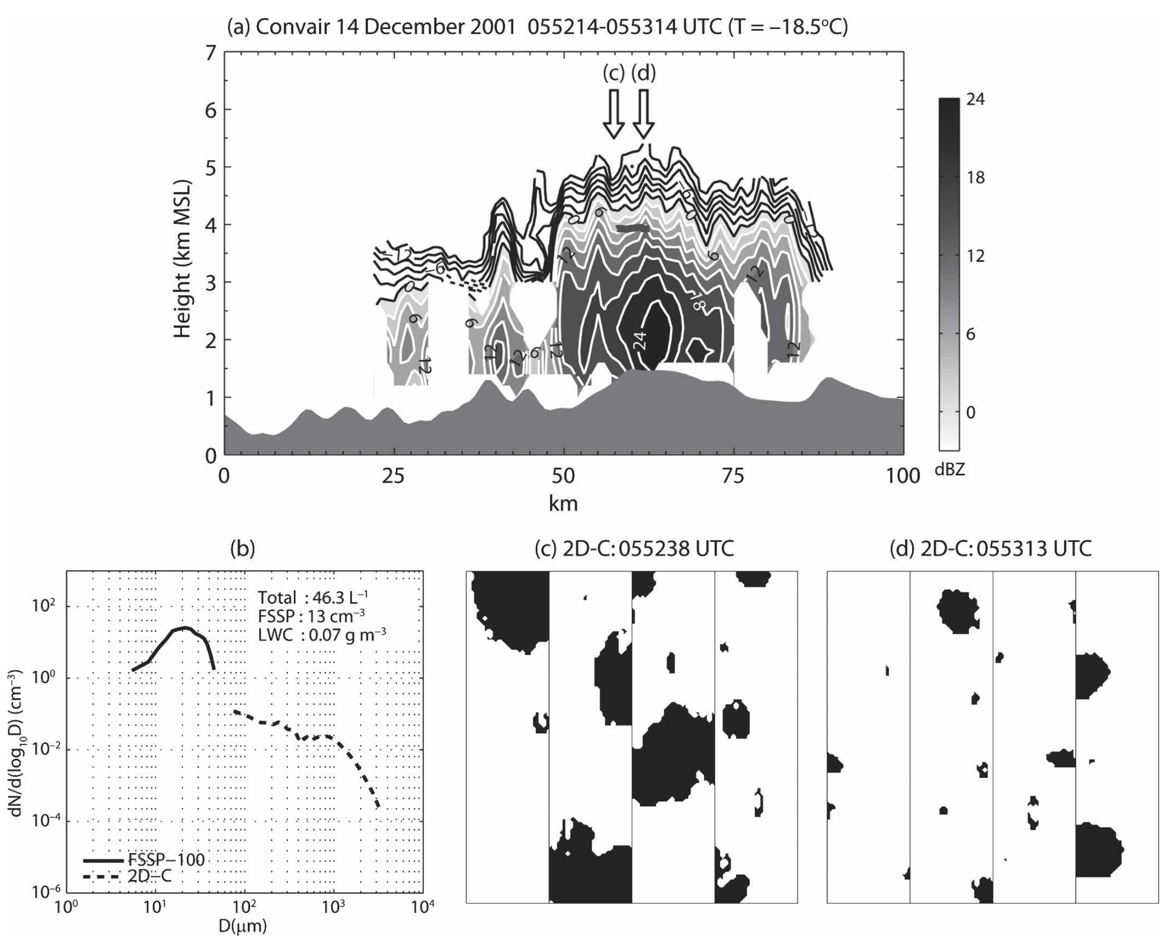

FIG. 23. Same as in Fig. 9, but for the Convair's ice particle observations between 0552:14 and 0553:14 UTC (bold horizontal line). The flight-level temperature is indicated. Holes in the reflectivity field are masked data affected by ground targets.

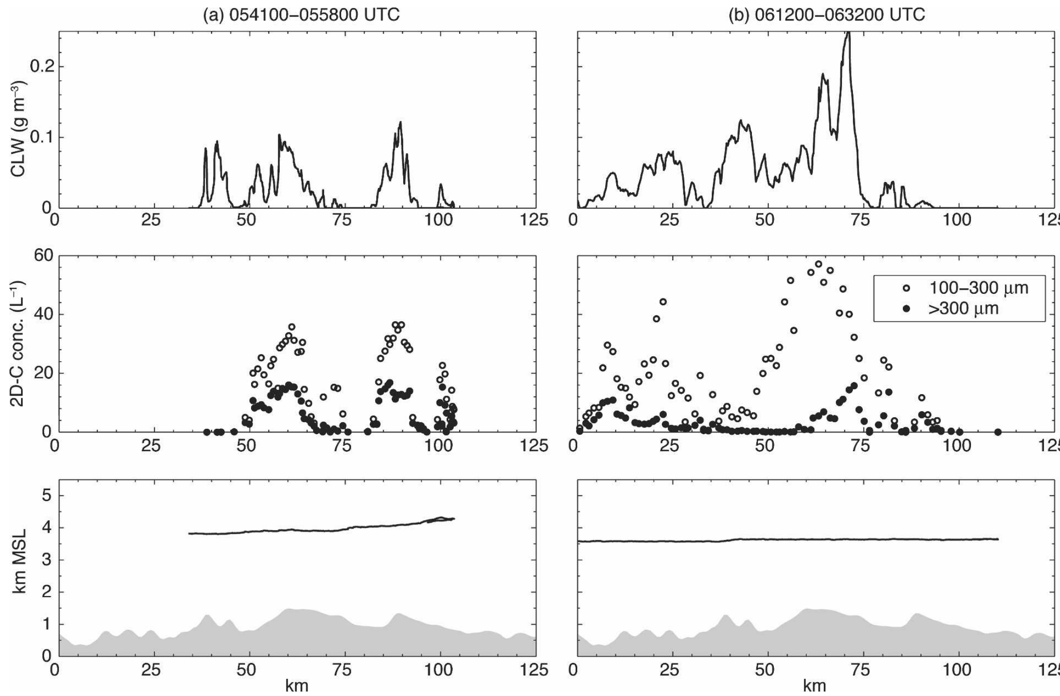

FIG. 24. (top) Cloud LWCs from the FSSP probe and (middle) concentrations of particles between 100- and 300-μm diameter and greater than 300-μm diameter based on the 2D-C data collected by the Convair during (a) 0541–0558 and (b) 0612–0632 UTC. (bottom) The terrain profiles and the flight altitudes.

5. Discussion

a. Microphysics

Observations of supercooled drizzle in the present case studies occurred most frequently in regions with 1) low ice concentrations, typically less than 1–2 L^{-1}; 2) low FSSP cloud droplet concentration, 15–50 cm^{-3}; 3) low CCN concentration, 15–30 cm^{-3}; and 4) cloud water content generally between 0.05 and 0.14 g cm^{-3} with local maxima between 0.2 and 0.4 g m^{-3}. In addition, the presence of large cloud drops (>40 μm) needed for the initiation of collision–coalescence was indicated by the bimodal FSSP spectra in some of these regions. These conditions are consistent with previous observations of drizzle formation in midlatitude storms of maritime origin (e.g., Hobbs 1975; Reynolds and Kuciauskas 1988; Rauber 1992). For example, Rauber (1992) found supercooled drizzle drops forming within a relatively warm topped (−15°C) orographic cloud over the Sierra Nevada. In the drizzle region studied by Rauber, the temperature was −5°C, the cloud liquid water content was 0.05–0.5 g m^{-3} with local maxima of 0.35–0.5 g m^{-3}, the FSSP concentration was 20–40 cm^{-3}, and the low ice concentration was indicated by a below-detection level of radar reflectivity (<0 dBZ). The formation of drizzle from a maritime cloud droplet spectrum (~50 cm^{-3}) has been shown by detailed microphysical modeling studies to typically require a cloud water mixing ratio of 0.20 g kg^{-1} or greater for the onset of autoconversion to drizzle drops (Feingold et al. 1996; Rasmussen et al. 2002). Consistent with the modeling studies, the air mass in the current cases were maritime with very low concentrations of cloud droplets and the cloud liquid water in the regions of drizzle observations was near the threshold values. Thus, given that the cloud top was fairly warm (>−19°C), the presence of drizzle is entirely reasonable.

The analyses of aircraft data from the current study showed that the presence or lack of supercooled drizzle was related to the balance between the condensate supply rate and the depletion of this supply rate. Ice crystals were observed to be the main cause for drizzle depletion. This can occur by depletion of the cloud water by depositional and riming growth of the ice crystals (reducing the cloud water content that grows drizzle), or by direct impaction of the drizzle drops on the ice crystals. Evidence for both of these processes was shown in the current case studies. If updrafts are sufficiently high as observed for these cases and cloud tops relatively warm (>−19°C in the current cases), the production rate of drizzle and liquid water can overcome its depletion by ice crystals, resulting in sustained regions of drizzle in the presence of the ice phase (mixed-phase regions). For instance, results from the 28 No-

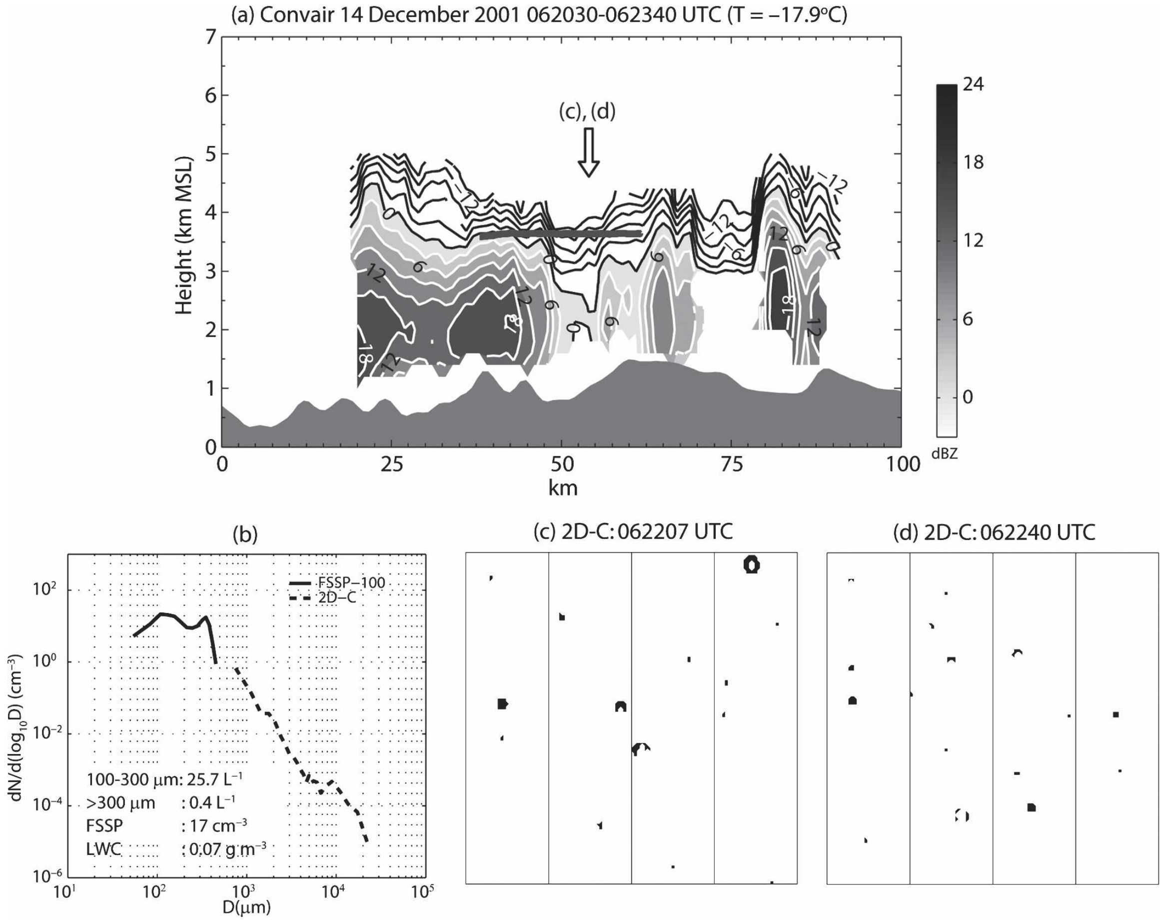

FIG. 25. Same as in Fig. 23 but for drizzle observations between 0620:30 and 0623:40 UTC. Drizzle (100–300 μm) and ice particle (>300 μm) concentrations are indicated in (b).

vember 2001 case showed that the significant upward motion over the mountain crest maintained a high condensate supply that slightly exceeded or balanced the depletion rate of liquid via depositional and/or accretional growth of ice crystals (section 3c). In this region, the condensate supply rate on the order of 1.0×10^{-3} g m^{-3} s^{-1} was estimated for the observed vertical motions of ~1.3 m s^{-1} (Rauber and Tokay 1991); while observed crystal concentration of 4 L^{-1} produced low depletion rates of 0.1–0.3×10^{-3} g m^{-3} s^{-1} from riming and 0.5–0.8×10^{-3} g m^{-3} s^{-1} from deposition. However, upwind of the mountain crest, the ascending motion generated by the smaller topographic ridges was not sufficient to overcome the depletion rate associated with the observed high ice concentrations (54 L^{-1}; Fig. 14). Ice crystals and snow particles in this region were carried downstream and formed graupel particles as they accreted supercooled liquid water at low levels. In contrast to the 28 November 2001 case, no significant concentration of drizzle drops were observed over the mountain crest for the 14 December 2001 case during the deep frontal precipitation period (section 4b). In this case, the high ice crystal concentrations from the deep cold-frontal cloud produced depletion rates of 3.0×10^{-3} g m^{-3} s^{-1}, overwhelming the condensate production rate of ~1.0×10^{-3} g m^{-3} s^{-1} produced by vertical motions of 1.5 m s^{-1}, despite relatively high cloud water content up to 0.2 g m^{-3}.

Similarly, comparisons of conditions found inside and outside of the weak convective turrets near the cloud top from the 28 November 2001 case (section 3b) and embedded convective cells within the postfrontal precipitation on 14 December 2001 (section 4d) revealed that convective turrets/cells produced significant ice concentrations suppressing the formation of drizzle-sized drops.

The main difference in the current cases compared with the previous observational studies of supercooled drizzle was the lower cloud-top temperatures (as low as −19° versus −15°C and higher typically observed in past studies), and the higher ice crystal concentration at flight levels [$<$1–2 versus $<$0.1 L^{-1} observed by Rasmussen et al. (1995) and Cober et al. (1996)]. One of the reasons that drizzle can exist at such low cloud temperatures may be the near balance of ice crystal fall speed between 0.5 and 1.0 m s^{-1} with the mean vertical motion over the barrier (0.5–1.0 m s^{-1}), leading to nearly terrain parallel trajectories of the ice particles as modeled by Hobbs (1975). In this case, the higher concentrations of ice particles at upper levels do not penetrate to the moisture-rich lower levels as easily (see, e.g., Fig. 8b). As a result, the amount of liquid lost through depletion is reduced, allowing supercooled water to accumulate over the windward barrier. When the horizontal wind is weaker ($\sim$25 m s^{-1}) and updraft weaker (0.2–0.4 m s^{-1}) as observed by Marwitz (1987), low-level moisture produced within the upslope flow is readily depleted by ice crystals descending into this layer from aloft. The relatively clean maritime air may also have lower concentrations of ice nuclei, suppressing the formation of ice.

The observed cloud water content over the barrier was found to form via three mechanisms: 1) general uplift over the topographic barrier with locally enhanced vertical motion (up to 2 m s^{-1}) above local ridges, 2) upward transport in convective updrafts, and 3) upward transport in embedded convection enhanced by flow over ridges. These mechanisms were also found to be active on the western slopes of the Washington Cascades (Hobbs 1975), the Tushar Mountains (Sassen et al. 1990), and the Wasatch Plateau (Huggins 1995) of Utah. In the currently examined cases, vertical motions were between 0.5 and 1.0 m s^{-1} with local maxima up to 2.0 m s^{-1} in the regions of cloud water maxima, significantly higher than the weak motions (0.03–0.5 m s^{-1}) observed in storms over the gradual slopes of the eastern Rockies (e.g., Rasmussen et al. 1995). Thus, the higher condensate supply rate was able to maintain cloud water contents sufficiently high and for prolonged periods of time to form drizzle in this maritime environment, and in part, it may have compensated for the relatively higher concentrations of ice observed in the drizzle regions as compared to the previous studies.

Another unique finding from our study, particularly from the 28 November 2001 case, is the observation of a significant supercooled drizzle in a region of relatively high reflectivity ($>$15 dBZ) associated with aggregates and rimed snow particles over the highest and steepest portion of the terrain (section 3c). In other regions, supercooled drizzle was associated with low reflectivity ($<$5 dBZ) consistent with Rauber (1992) and other studies, and as expected from small sizes of the drizzle drops. This finding shows the importance of understanding the impact of local topography enhancements in condensate supply rate when interpreting the radar returns for icing hazard potential.

b. Drizzle locations in relation to storm evolution

The two extratropical cyclones examined in this study (Figs. 1 and 26) closely followed the split-front model of Browning and Monk (1982). In the current case studies, the conditions conducive to the formation of supercooled drizzle occurred during two particular stages of the cyclones. Drizzle was observed in the intrafrontal period immediately following the passage of the upper cold/humidity fronts (Fig. 26b) and in the postfrontal period (Figs. 26c,d). In the former period, the seeder portion of the cloud system was eliminated by the passage of the upper dry cold front, allowing drizzle to form in the warm, moisture-rich orographic cloud without depletion by ice crystals from aloft. Freezing drizzle was observed during this same stage of Sierra Nevada split-front storms by Reynolds and Kuciauskas (1988).

In the postfrontal period, supercooled drizzle prevailed between the weak convective turrets (section 3b; Fig. 26c), between shallow low-level convective cores embedded within the orographic cloud (section 4d; Fig. 26d), and over the mountain crest where the vertical motion was significantly amplified (section 3c; Fig. 26d).

Supercooled drizzle drops have been observed between weak convective turrets within a warm-frontal cloud by Field et al. (2004) with a small-ice detector on a research aircraft and the 3-GHz Chilbolton Advanced Meteorological Radar. Similar to the current case, high ice crystal concentrations readily depleted supercooled liquid water and drizzle within the turrets. The formation of supercooled liquid drops outside the turrets was attributed by Field et al. to be most likely related to the production of supercooled liquid by the frontal lifting and the low loss rate of liquid to ice in these regions due to the low concentrations of ice crystals as in the present cases. Sassen et al. (1990) observed similar depletion of supercooled liquid water within embedded convective cells over the Tushar Mountains, attributed to the sweeping out of the supercooled liquid water by the ice particles. The turret temperatures in his case were $-14°$ to $-17°$C, similar to the 28 November 2001 case. The observations from the two current case studies are also consistent with a long-term study of winter storms over the Washington Cascades by Hobbs (1975) in which frozen drops were commonly observed at the ground within postfrontal shallow orographic clouds

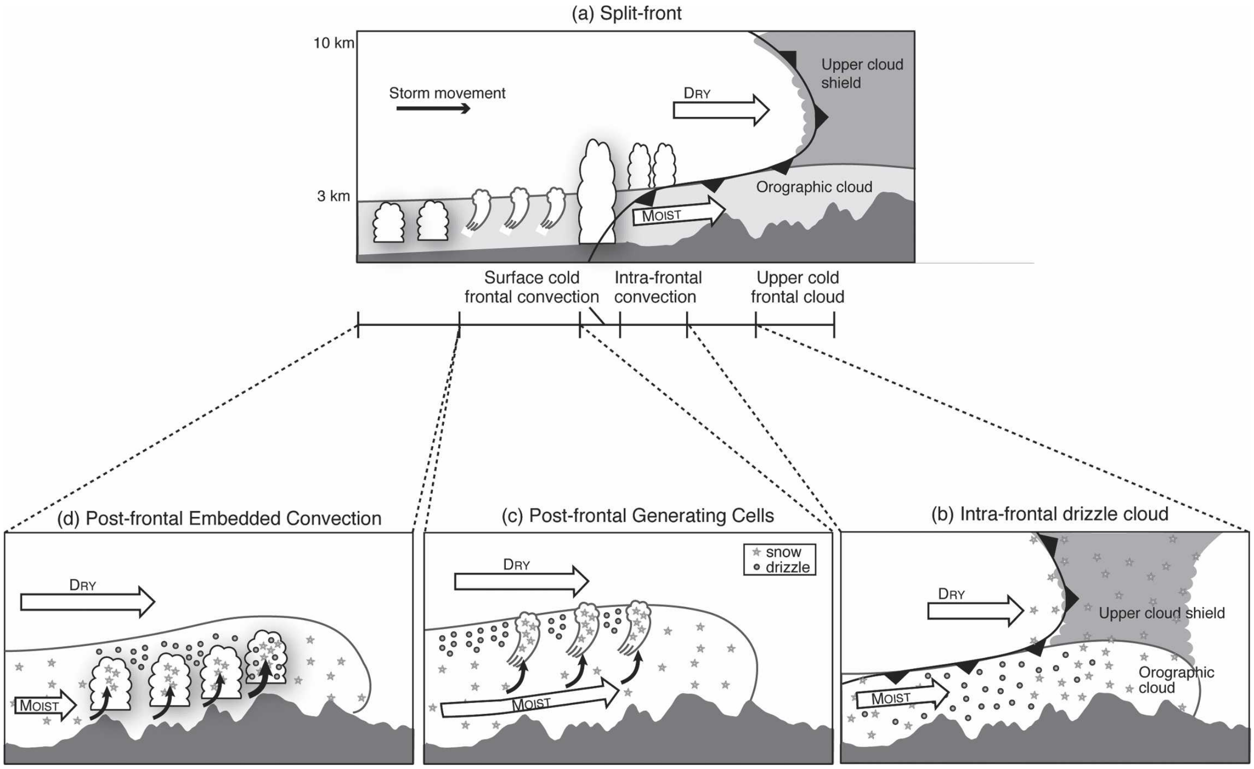

FIG. 26. (a) Schematic diagram of clouds associated with various stages of a split-front system interacting with a mountain barrier. (b)–(d) Closeups of (a), showing moist airflow over the mountain barrier (open arrow in the orographic cloud layer), enhanced vertical motions initiated by local topographic ridges (solid black arrows), and dry air aloft (open arrow above the orographic cloud). Also indicated are the locations of freezing drizzle (circles) and ice particles (stars) corresponding with the individual storm stages. Stage 5 (postfrontal convection) noted in section 1 is divided into two stages [(c) and (d)] to correspond with the two storms detailed in this study.

(cloud-top temperature typically greater than $-15°C$), in which clouds were often not completely glaciated even at temperatures as low as $-18°C$.

Observations from cases with stronger embedded convection and at warmer temperatures indicate that supercooled liquid water and drizzle are not always depleted within embedded convection, but may depend on the vertical velocity and temperature. Hauf and Shröder (2006) observed the presence of supercooled drizzle drops in embedded convection with updraft velocities of 5 $m\,s^{-1}$ and a cloud-top temperature near $-11°C$. In this case, the high condensate supply rate generated by the strong vertical velocity was likely able to overwhelm the depletion of supercooled water and drizzle by ice crystals. Another factor may be the factor of 10 lower diffusional growth rate of crystals at water-saturated conditions at $-10°C$ as compared to at $-15°C$ (Pruppacher and Klett 1997). Observations from Baddour and Rasmussen (1989) of embedded convection clouds associated with a winter storm in Morocco also showed the presence of supercooled liquid water and drizzle within embedded convection. In their case, the vertical velocity was also relatively strong (4–6 $m\,s^{-1}$) as in Hauf and Shröder (2006) and the temperature relatively high (near $-10°C$). Thus, whether supercooled drizzle is present within embedded convection seems to be correlated with the strength of the vertical velocity (an indication of condensate supply rate) and to the temperature of the embedded convection (lower temperatures produce higher ice crystal concentrations as well as higher depletion rates. In the current case, weaker vertical velocities (1–2 $m\,s^{-1}$) and colder temperatures ($-15°$ to $-19°C$) associated with convective turrets/cells produced relatively low condensate supply rates and high depletion rates, preventing the formation of supercooled drizzle aloft within embedded convection.

The observation of enhanced ice formation in the embedded convection (factor of 10 higher concentration than outside the embedded convection) suggests that supersaturation above water may play an important role in the formation of ice crystals in these clouds as found in previous studies, especially in laboratory studies (Pruppacher and Klett 1997), since the temperature was nearly the same within and outside the embedded convection. Since the embedded convection was surrounded by water-saturated cloud, ice formation processes related to evaporation are likely not active.

c. Reasons for the low ice crystal concentration in the shallow orographic clouds

Since the air mass is coming from the ocean, and the CCN concentration is very low, we characterize the air mass from which the cloud is forming as maritime. Observations from Rangno and Hobbs (1988, 1991) and Hobbs and Rangno (1985, 1990) indicate that ice formation begins near the cloud top in maritime clouds, where drizzle drops also appear at concentrations of a few per liter. These drizzle drops freeze and begin to rime by collecting cloud droplets of diameter greater than 20 μm. This is followed by the appearance of largely vapor grown crystals, in concentration of 10–100 L^{-1}. These crystals in turn freeze more drizzle drops, so a rapidly accelerating ice generation process occurs, producing high concentrations of ice crystals within 10 min. Rather than correlating with cloud-top temperature, the maximum ice crystal concentration ($N_{IC,max}$) was correlated with the size of the drops (D_0) in the cloud with the following equation:

$$N_{IC,max} = (D_T/D_0)^{\eta}, \qquad (1)$$

with $D_0 = 18.5$ μm and $\eta = 8.4$ for cumuliform clouds, and $D_0 = 19.4$ μm and $\eta = 6.6$ for stratiform clouds, where D_T is a threshold diameter defined such that drops of $D_0 > D_T$ appear in a total concentration of 3 cm^{-3}.

The above conditions fit with the microphysical character and measurements in the postfrontal shallow orographic clouds in the current study. One of the main discrepancies, however, is the lack of ice crystals in the freezing drizzle region outside of the embedded convection regions. The only possible broken link in the ice crystal enhancement chain described above is the initial freezing of the drizzle drops. Thus, the key question is why the drizzle drops did not freeze despite existing at temperatures as cold as $-19°C$. One possibility is the depletion of ice nuclei upstream of the cloud due to the nucleation of ice crystals, and fallout of the nucleated ice crystals. The remaining cloud droplets and drizzle drops would be those not containing ice nuclei. Thus, regions downstream of the ice crystal fall region would primarily consist of unfrozen cloud and drizzle drops. Simple calculations suggest that ice crystals nucleated in the upstream shallow cloud (1 km thick), would fall out in 1500 s given a fall speed of 1 m s^{-1} and mean cloud updraft of 0.5 m s^{-1}. Assuming a mean wind speed of 35 m s^{-1}, crystals would fall out within 50 km of initiation at cloud top. Given the 100-km length of the barrier, the portion of the cloud 50 km upstream of the mountain crest would likely be relatively devoid of ice crystals. In fact, the crystals would not have to fall very far to leave the upper regions of the cloud ice nuclei free, allowing unfrozen drizzle drops to exist. A 2D orographic modeling study using a detailed microphysical parameterization by Rasmussen et al. (2002) found a similar result; if ice nuclei were not depleted upstream, unfrozen drizzle drops did not form due to the drizzle drops freezing. The current observations appear to be consistent with this scenario. This behavior may also help explain the weaker ice enhancement observed by Rangno and Hobbs (1991) and Hobbs and Rangno (1990) (as described in the equation above) for stratiform clouds as compared to cumulus clouds.

The current observations also showed enhanced ice crystal formation in regions of embedded convection near the cloud top within the shallow orographic cloud (section 3b). In this case, ice nuclei may be entrained into the cloud from above the cloud due to the convective motions, allowing the drizzle drops to freeze and start the ice formation process. Another possibility is the creation of ice via enhanced supersaturation in the convective cloud (Pruppacher and Klett 1997).

6. Summary and conclusions

Observations of supercooled drizzle were examined from two storms impacting the Oregon Cascades. Drizzle formed through a condensation and collision–coalescence process in a maritime air mass having liquid water contents up to ~0.2 g m^{-3}, and ice crystal concentrations less than 1–2 L^{-1}. Previous studies found most occurrences of freezing drizzle to be associated with cloud-top temperatures of $-15°C$ or higher (Geresdi et al. 2005) and ice concentrations lower than 0.1 L^{-1}. In the current cases, freezing drizzle was found in clouds with cloud-top temperatures as low as $-19°C$ containing a relatively higher concentration of ice crystals. Suggested reasons for the presence of drizzle in such environments were 1) the higher condensate supply rate induced by the topography (strong flow in both storms); 2) the lower influx of ice crystals from upper levels due to the absence of upper-level seeder clouds or as a result of the balance of ice crystal terminal velocity with large upward motion; and/or 3) the suppression of ice nucleation in the clean maritime air.

The low ice crystal concentration in regions of freezing drizzle observed in the current case is counterintuitive to previous observations by Rangno and Hobbs (1991) and Hobbs and Rangno (1990) that indicate that high ice crystal concentrations should be present in these types of maritime clouds when drizzle and large cloud droplets are present. We hypothesize that ice nuclei depletion upstream of the region due to the fall out of any nucleated ice crystals is the cause for this behavior, allowing drizzle to supercool without freezing. The high concentration in the generating cells near the cloud top are likely due to the entrainment of ice nuclei from above cloud, or via enhanced ice nucleation via supersaturation.

The two storms conformed to the split-frontal model discussed by Browning and Monk (1982), a storm type that is frequently observed over the Sierra Nevada and Washington Cascade mountains (e.g., Reynolds and Kuciauskas 1988). Freezing drizzle occurred during distinct stages of these storms (Fig. 26): 1) the intrafrontal period on 14 December 2001 during which the combination of the loss of a seeder cloud aloft and prevalence of warm moist low-level cloud allowed drizzle drops to form; and 2) the postfrontal period in which drizzle was observed in both cases to occur between generating turrets or low-level convective cores. This latter result is in agreement with a number of previous orographic and frontal cases with embedded convection. In contrast, a number of previous studies of stronger embedded convection at warmer temperatures found supercooled water and drizzle preferentially to occur within the convective cells. The difference between these warmer and more vigorous cases and the current colder and weaker cases may be attributed to the relatively higher concentration of ice crystal inside the current convective cells and the higher depositional growth rates at $-15°C$ as compared to $-10°C$, and the relatively weaker convective updrafts in the current cases (1–2 versus 5 m s^{-1}) which reduces the condensate supply rate, allowing the liquid water and drizzle to be depleted more than in the stronger updraft cases.

Unique to this study was an observation of supercooled drizzle in regions of relatively strong radar reflectivity (>15 dBZ) owing to the presence of snow aggregates that coexisted with significant amounts of supercooled drizzle on 28 November 2001. In this case, the depletion rate of water by ice particles entering into this region was not sufficient to deplete the cloud water and drizzle. The combination of a continuous supply of low-level moisture as discussed above and a large residence time provided from the terrain generated sufficient vertical velocity to allow the conversion of cloud water to drizzle drops without depletion. The current case studies reveal that vertical motions generated by both large-scale and local topographic features are critical in precipitation processes such as drizzle formation and thus it is essential that microphysical models predict these motions.

Acknowledgments. The authors are grateful to Drs. Peter Hobbs, Mark T. Stoelinga, and Bradley F. Smull, Nicholas Bond, and Matthew Garvert for providing us with essential field datasets, and the flight crews of the NOAA P-3 and the UW Convair for their detailed flight notes. The kind efforts of Robert A. Rilling of NCAR for preparing the radar data are greatly appreciated. The authors would also like to thank Kristen Rasmussen for her assistance in data analyses. Suggestions from anonymous reviewers are greatly appreciated. This work was supported by the NCAR U.S. Weather Research Program, NCAR Water Cycle Across Scales initiative, and Federal Aviation Weather Research Program. The views expressed are those of the authors and do not necessarily represent the official policy of the U.S. government.

REFERENCES

Ashenden, R., W. Lindberg, J. D. Marwitz, and B. Hoxie, 1996: Airfoil performance degradation by supercooled cloud, drizzle, and rain drop icing. *J. Aircraft,* **33,** 1040–1046.

Baddour, O., and R. M. Rasmussen, 1989: Microphysical observations in winter storms over the Atlas Mountains in Morocco. *Atmos. Res.,* **24,** 103–122.

Bernstein, B. C., 2000: Regional and local influences on freezing drizzle, freezing rain, and ice pellet events. *Wea. Forecasting,* **15,** 485–508.

——, T. A. Omeron, F. McDonough, and M. K. Politovich, 1997: The relationship between aircraft icing and synoptic-scale weather conditions. *Wea. Forecasting,* **12,** 742–762.

——, ——, M. K. Politovich, and F. McDonough, 1998: Surface weather features associated with freezing precipitation and severe in-flight aircraft icing. *Atmos. Res.,* **46,** 57–74.

——, F. McDonough, M. K. Politovich, B. G. Brown, T. P. Ratvasky, D. R. Miller, C. A. Wolff, and G. Cunning, 2005: Current icing potential: Algorithm description and comparison with aircraft observations. *J. Appl. Meteor.,* **44,** 969–986.

Browning, K. A., and G. A. Monk, 1982: A simple model for the synoptic analysis of cold fronts. *Quart. J. Roy. Meteor. Soc.,* **108,** 435–452.

Cober, S. G., J. W. Strapp, and G. A. Isaac, 1996: An example of supercooled drizzle drops formed through a collision–coalescence process. *J. Appl. Meteor.,* **35,** 2250–2260.

——, G. A. Isaac, and J. W. Strapp, 2001: Characterizations of aircraft icing environments that include supercooled large drops. *J. Appl. Meteor.,* **40,** 1984–2002.

Cortinas, J. V., Jr., B. C. Bernstein, C. C. Robbins, and J. W.

Strapp, 2004: An analysis of freezing rain, freezing drizzle, and ice pellets across the United States and Canada: 1976–1990. *Wea. Forecasting,* **19,** 377–390.

Feingold, G., S. M. Kreindenweis, B. Stevens, and W. R. Cotton, 1996: Numerical simulations of stratocumulus processing of cloud condensation nuclei through collision-coalescence. *J. Geophys. Res.,* **101,** 21 391–21 402.

Field, P. R., R. J. Hogan, P. R. A. Brown, A. J. Illingworth, T. W. Choularton, P. H. Kaye, E. Hirst, and R. Greenaway, 2004: Simultaneous radar and aircraft observations of mixed-phase cloud at the 100 m scale. *Quart. J. Roy. Meteor. Soc.,* **130,** 1877–1904.

Garvert, M. F., B. A. Colle, and C. F. Mass, 2005: The 13–14 December 2001 IMPROVE-2 event. Part I: Synoptic and mesoscale evolution and comparison with a mesoscale model simulation. *J. Atmos. Sci.,* **62,** 3431–3455.

Geresdi, I., R. M. Rasmussen, and W. Grabowski, 2005: Sensitivity of freezing drizzle formation in stably stratified clouds to ice processes. *Meteor. Atmos. Phys.,* **88,** 91–105.

Hauf, T., and F. Shröder, 2006: Aircraft icing research flights in embedded convection. *Meteor. Atmos. Phys.,* **91,** 247–265.

Heggli, M. F., and D. W. Reynolds, 1985: Radiometric observations of supercooled liquid water within a split front over the Sierra Nevada. *J. Climate Appl. Meteor.,* **24,** 1258–1261.

——, and R. M. Rauber, 1988: The characteristics and evolution of supercooled water in wintertime storms over the Sierra Nevada: A summary of radiometric measurements taken during the Sierra Cooperative Pilot Project. *J. Appl. Meteor.,* **27,** 989–1015.

Hobbs, P. V., 1975: The nature of winter clouds and precipitation in the Cascade Mountains and their modification by artificial seeding. Part I: Natural conditions. *J. Appl. Meteor.,* **14,** 783–804.

——, and A. L. Rangno, 1985: Ice particle concentrations in clouds. *J. Atmos. Sci.,* **42,** 2523–2549.

——, and ——, 1990: Rapid development of high ice particle concentrations in small polar maritime cumuliform clouds. *J. Atmos. Sci.,* **47,** 2710–2722.

Huggins, A. W., 1995: Mobile microwave radiometer observations: Spatial characteristics of supercooled cloud water and cloud seeding implications. *J. Appl. Meteor.,* **34,** 432–446.

Ikeda, K., E. A. Brandes, and R. M. Rasmussen, 2005a: Polarimetric radar observation of multiple freezing levels. *J. Atmos. Sci.,* **62,** 3624–3636.

——, R. M. Rasmussen, and E. A. Brandes, 2005b: Freezing drizzle detection with WSR-88D radars. Preprints, *12th Conf. on Aviation Range and Aerospace Meteorology,* Atlanta, GA, Amer. Meteor. Soc., CD-ROM, 7A.2.

Isaac, G. A., S. G. Cober, A. V. Korolev, J. W. Strapp, and A. Tremblay, 1999: Canadian Freezing Drizzle Experiment. *Extended Abstracts, 37th AIAA Aerospace Science Meeting and Exhibit,* AIAA Paper 99-0492, Reno, NV, American Institute of Aeronautics and Astronautics, 10 pp.

——, ——, J. W. Strapp, A. V. Korolev, A. Tremblay, and D. L. Marcotte, 2001: Recent Canadian research on aircraft inflight icing. *Can. Aeronaut. Space J.,* **47,** 213–221.

Korolev, A. V., J. W. Strapp, and G. A. Isaac, 1998: Evaluation of the accuracy of PMS optical array probes. *J. Atmos. Oceanic Technol.,* **15,** 708–720.

Marwitz, J. D., 1987: Deep orographic storms over the Sierra Nevada. Part II: The precipitation processes. *J. Atmos. Sci.,* **44,** 174–185.

Miller, D., T. Ratvasky, B. C. Bernstein, F. McDonough, and J. W. Strapp, 1998: NASA/FAA/NCAR supercooled large droplet icing flight research: Summary of winter 96-97 flight operations. *Extended Abstracts, 36th AIAA Aerospace Science Meeting and Exhibit,* AIAA Paper 98-0557, Reno, NV, American Institute of Aeronautics and Astronautics, 20 pp.

Murakami, M., Y. Yamada, T. Matsuo, H. Mizuno, and K. Morikawa, 1992: Microphysical structures of warm-frontal clouds. The 20 June 1987 case study. *J. Meteor. Soc. Japan,* **70,** 877–895.

Neiman, P. J., G. A. Wick, F. M. Ralph, B. E. Martner, A. B. White, and D. E. Kingsmill, 2005: Wintertime nonbrightband rain in California and Oregon during CALJET and PACJET: Geographic, interannual, and synoptic variability. *Mon. Wea. Rev.,* **133,** 1199–1223.

Politovich, M. K., 1989: Aircraft icing caused by large supercooled droplets. *J. Appl. Meteor.,* **28,** 856–868.

Pruppacher, H. R., and J. D. Klett, 1997: *Microphysics of Clouds and Precipitation.* 2d ed. Kluwer Academic Publishers, 954 pp.

Rangno, A. L., and P. V. Hobbs, 1988: Criteria for the development of significant concentrations of ice particles in cumulus clouds. *Atmos. Res.,* **21,** 1–13.

——, and ——, 1991: Ice particle concentrations and precipitation development in small polar maritime cumuliform clouds. *Quart. J. Roy. Meteor. Soc.,* **117,** 207–241.

Rasmussen, R. M., P. Smolarkiewicz, W. D. Hall, and T. Clarks, 1988: Comparison of orographic cloud and precipitation development of three different geographic locations using a 3-D nested grid cloud model. Preprints, *10th Int. Cloud Physics Conf.,* Hamburg, Germany, IAMAP/ICCP, 353–355.

——, and Coauthors, 1992: Winter Icing and Storms Project (WISP). *Bull. Amer. Meteor. Soc.,* **73,** 951–974.

——, B. C. Bernstein, M. Murakami, G. Stossmeister, and B. Stankov, 1995: The 1990 Valentine's Day arctic outbreak. Part I: Mesoscale and microscale structure and evolution of a Colorado Front Range shallow upslope cloud. *J. Appl. Meteor.,* **34,** 1481–1511.

——, I. Geresdi, G. Thompson, K. Manning, and E. Karplus, 2002: Freezing drizzle formation in stably stratified layer clouds: The role of radiative cooling of cloud droplets and cloud condensation and ice initiation. *J. Atmos. Sci.,* **59,** 837–860.

Rauber, R. M., 1992: Microphysical structure and evolution of a central Sierra Nevada orographic cloud system. *J. Appl. Meteor.,* **31,** 3–24.

——, and A. Tokay, 1991: An explanation for the existence of supercooled water at the top of cold clouds. *J. Atmos. Sci.,* **48,** 1005–1023.

——, L. S. Olthoff, M. K. Ramamurthy, and K. E. Kunkel, 2000: The relative importance of warm rain and melting processes in freezing precipitation events. *J. Appl. Meteor.,* **39,** 1185–1195.

Reynolds, D. W., and A. P. Kuciauskas, 1988: Remote and in situ observations of Sierra Nevada winter mountain clouds: Relationships between mesoscale structure, precipitation, and liquid water. *J. Appl. Meteor.,* **27,** 140–156.

Sand, W. R., W. A. Cooper, M. K. Politovich, and D. L. Veal, 1984: Icing conditions encountered by a research aircraft. *J. Climate Appl. Meteor.,* **23,** 1427–1440.

Sassen, K., A. W. Huggins, A. B. Long, J. B. Snider, and R. J.

Mettín, 1990: Investigations of a winter mountain storm in Utah. Part II: Mesoscale structure, supercooled liquid water development, and precipitation processes. *J. Atmos. Sci.,* **47,** 1323–1350.

Stoelinga, M. T., and Coauthors, 2003: Improvement of microphysical parameterization through observational Verification Experiment. *Bull. Amer. Meteor. Soc.,* **84,** 1807–1826.

Strapp, J. W., J. Oldenburg, R. Ide, Z. Vukovic, S. Bacic, and L. Lilie, 2000: Measurements of the response of hot wire LWC and TWC probes to large droplet clouds. Preprints, *13th Conf. on Clouds and Precipitation,* Reno, NV, Amer. Meteor. Soc., 181–184.

Telford, J. W., 1988: An example of the behavior of an aircraft with accumulated ice: Latent instability. *J. Appl. Meteor.,* **27,** 1093–1108.

Woods, C. P., M. T. Stoelinga, J. D. Locatelli, and P. V. Hobbs, 2005: Microphysical processes and synergistic interaction between frontal and orographic forcing of precipitation during the 13 December 2001 IMPROVE-2 event over the Oregon Cascades. *J. Atmos. Sci.,* **62,** 3493–3519.